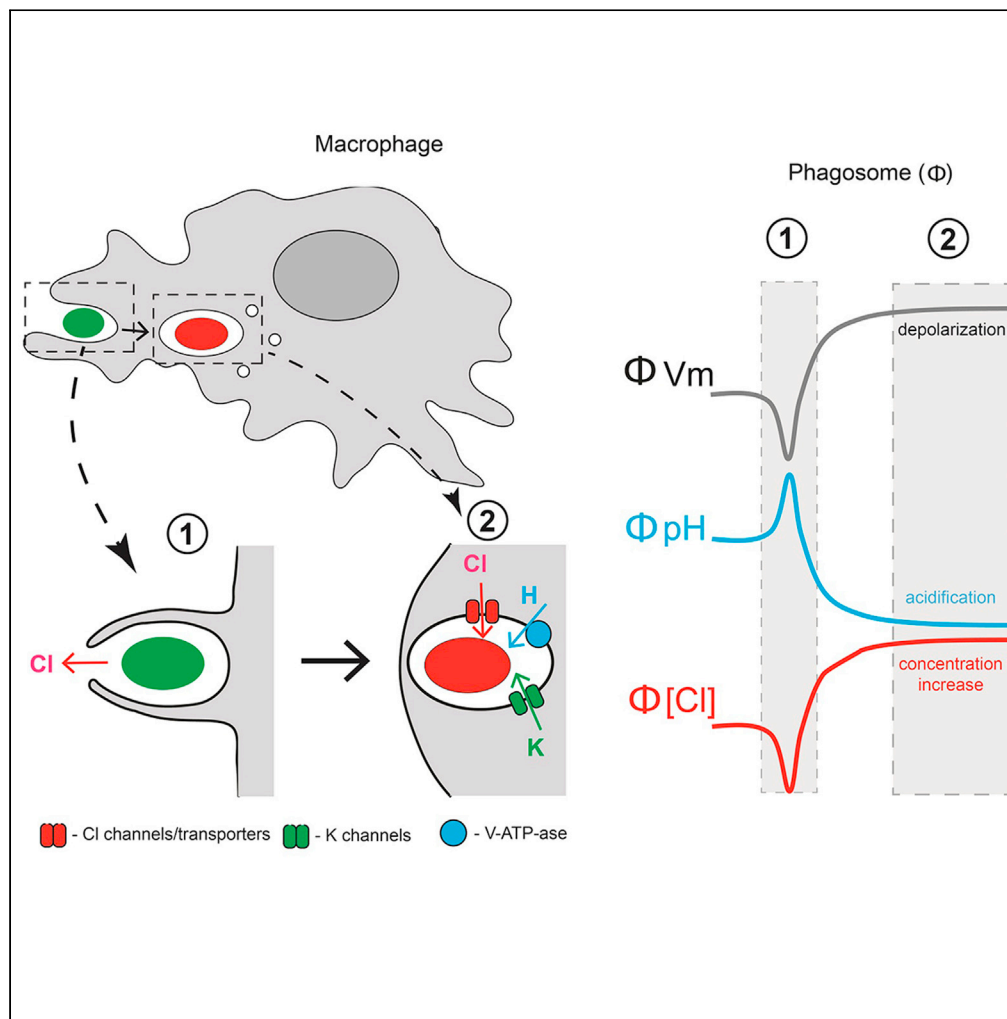# iScience

Article

Phagosomal chloride dynamics in the alveolar macrophage

Vladimir Riazanski,
Gerardo Mauleon,
Adriana M.
Zimnicka, Si Chen,
Deborah J. Nelson

nelson@uchicago.edu

Highlights

Cl^- provides the main phagosomal shunt conductance determining the acidic pH

CFTR and CLC channels comprise the Cl^- conductance influx pathway in AM phagosomes

The biphasic $[Cl^-]$ kinetics: A brief efflux than influx drive pH and K^+ changes

Mature phagosomal $[Cl^-]$ saturates at 190–200 mM driven by the E_{Cl} potential

Article

Phagosomal chloride dynamics in the alveolar macrophage

Vladimir Riazanski,[1] Gerardo Mauleon,[1] Adriana M. Zimnicka,[1] Si Chen,[2] and Deborah J. Nelson[1,3,*]

SUMMARY

Acidification in intracellular organelles is tightly linked to the influx of Cl⁻ counteracting proton translocation by the electrogenic V-ATPase. We quantified the dynamics of Cl⁻ transfer accompanying cargo incorporation into single phagosomes in alveolar macrophages (AMs). Phagosomal Cl⁻ concentration and acidification magnitude were followed in real time with maximal acidification achieved at levels of approximately 200 mM. Live cell confocal microscopy verified that phagosomal Cl⁻ influx utilized predominantly the Cl⁻ channel CFTR. Relative levels of elemental chlorine (Cl) in hard X-ray fluorescence microprobe (XFM) analysis within single phagosomes validated the increase in Cl⁻ content. XFM revealed the complex interplay between elemental K content inside the phagosome and changes in Cl⁻ during phagosomal particle uptake. Cl⁻ -dependent changes in phagosomal membrane potential were obtained using second harmonic generation (SHG) microscopy. These studies provide a mechanistic insight for screening studies in drug development targeting pulmonary inflammatory disease.

INTRODUCTION

In the intracellular vesicle space, acidification drives function. Acidification is directly dependent upon the activity of the vesicular ATPase responsible for the accumulation of protons in the restricted vesicular luminal compartments. Lysosomal pH is perhaps the most acidic of the vesicular compartments ensuring an optimum degradative enzyme environment of approximately pH 4.5 (Mindell, 2012). The membranes of intracellular vesicles including endosomes, lysosomes, and phagosomes as well as synaptic vesicles and secretory granules share common ion channels and transporters in their limiting membranes. Ion channel gating serves to move ions in a direction needed to reduce the positive potential that develops as protons are translocated into the vesicle lumen. Movement of counter ions down their electrochemical gradient in response to V-ATPase activity serves as a charge shunt, enabling and ensuring continued proton pump activity which would otherwise create a self-limiting lumen positive potential. The identity of the charge shunt has been attributed to either channel-mediated anion influx or cation efflux. Membrane transporters, including the Na/H exchanger and the rheogenic exchangers of the ClC family of Cl⁻ transport proteins, as well as the Cl⁻ channel CFTR (**C**ystic **F**ibrosis **T**ransmembrane conductance **R**egulator) function as charge shunts, modulating functional states as well (Hackam et al., 1997) (Di et al., 2006) (Wang, 2016) (Jentsch and Pusch, 2018). Ion channels responsible for the heterogeneous charge shunt pathways are both targeted to a specific vesicle population and accumulated stochastically into the vesicle resultant to endosomal plasma membrane uptake. Highly selective ion channels may facilitate movement of ions both in and out of vesicles depending upon the dynamic changes in vesicle membrane potential following vesicle formation and the ionic gradients set up between cytoplasm and vesicle interior. Only recently has the technique of electrophysiology allowed the measurement of current flow directly in single isolated vesicles and revealed vesicle currents generated by channels of the transient receptor potential (TRP) family which appear cation selective, both monovalent and divalent (Dong et al., 2008) (Wang et al., 2012) (Samie et al., 2013) (Chen et al., 2017) (Wang et al., 2017).

Vesicles in the endocytic pathway derive their spectrum of ion transport elements both from the plasma membrane and the fusion of resident cytoplasmic vesicle populations as recently reviewed by Chadwick et al (Chadwick et al., 2021). In this investigation, we have chosen to focus on the phagosomal compartment that is formed during the engulfment of zymosan as a surrogate for bacterial cargo destined for a microbicidal endpoint via both oxidative and non-oxidative metabolism as recently examined by Riazanski

[1]The University of Chicago, Department of Pharmacological and Physiological Sciences, 947 E. 58th Street, MC 0926, Chicago, IL 60637, USA

[2]X-ray Science Division, Advanced Photon Source, Argonne National Laboratory, Argonne, IL 60439, USA

[3]Lead contact

*Correspondence:
nelson@uchicago.edu

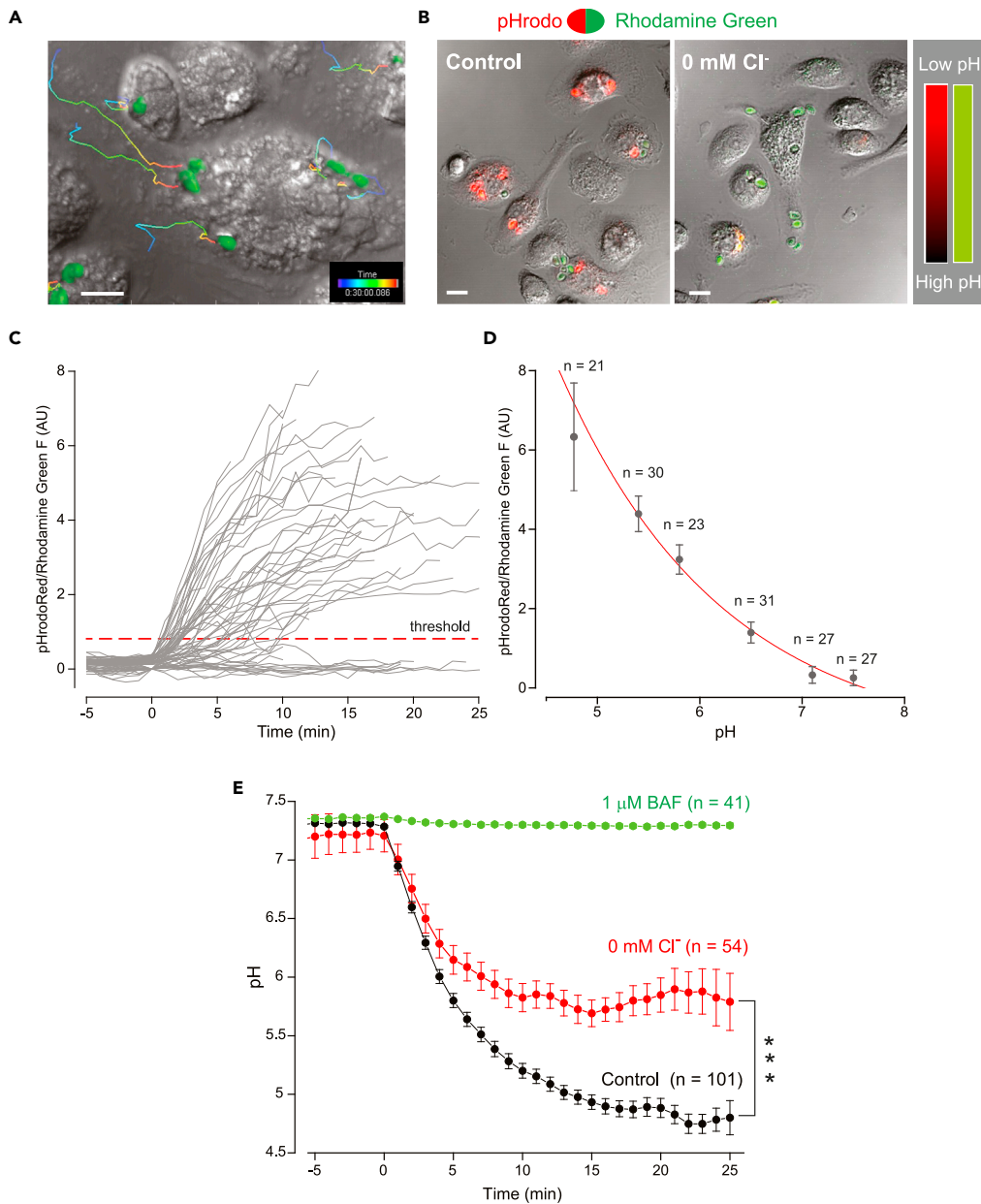https://doi.org/10.1016/j.isci.2021.103636

Figure 1. Chloride dependence of phagosomal acidification

(A) A representative composite image (gray - DIC; green - rendered Rhodamine Green signal) of an Imaris tracking in 3D volume over time of doubly labeled with Rhodamine Green and pHrodo Red zymosan particles during phagocytosis (shown in rendered form with coloration according to tracking time of "tail" lines) by AMs in DIC (scale bar, 10 μm, rainbow timescale).

(B) Representative composite images (gray - DIC; red – pHrodo Red; green – Rhodamine Green) of AMs obtained at 30 min after adding doubly labeled zymosan particles for tracking phagosomal pH changes in control media containing 131.5 mM Cl⁻ (Control) and Cl⁻–free media (0 mM Cl⁻). Lookup tables on the right indicate relative changes in pHrodo Red and Rhodamine Green color channel intensity in relation to pH change. Scale bar 10 μm.

(C) Overlaid representative traces of the time dependence of individual fluorescence intensity change ratios: pHrodo Red/Rhodamine Green in phagosomes from AMs in Cl⁻- free media in a time period of 25 min. Dotted red line indicates an arbitrary cutoff amplitude threshold used for determining "acidifying" and "non-acidifying" traces.

(D) pH-dependent fluorescence changes for zymosan particles doubly labeled with the pH-sensitive dye pHrodo Red and pH-insensitive Rhodamine Green. The calibration curve was obtained by fitting data with an exponential decay fit $(y = A1*exp(-x/t1) + y0)$. Numbers represent numbers of doubly labeled zymosan particles measured per pH value.

Figure 1. *Continued*

(E) Phagosomal acidification timecourse in AMs in control media (black trace, Control, n = 101 particles, 89 cells, 3 mice) pH at 24 min: 4.78 ± 0.1, in Cl⁻-free media (red trace, n = 54 particles, 48 cells, 3 mice) pH at 24 min: 5.82 ± 0.24, in the presence of 1 μM bafilomycin (green trace, BAF, n = 41 particles, 18 cells, 3 mice) pH at 24 min: 7.29 ± 0.01, measured with doubly labeled zymosan particles (pHrodo Red and Rhodamine Green). Data are represented as mean ± SEM. Significance level determined by One-Way ANOVA Tukey test (***p<0.001).

et al (Riazanski et al., 2020). Chloride ion (Cl⁻) influx through phagosomal membrane anion channels has a prominent role in the production not only of degradative intermediates including hypochlorous acid but also the production of an acidic environment that is favorable for enzymatic activity contributed by the fusion of lysosomal contents (Di et al., 2006) (Wang, 2016) (Riazanski et al., 2015). Open questions surrounding the role of Cl⁻ anions in the metabolic activity of the degradative phagosome include: estimates of the magnitude of the concentration change in Cl⁻ during a functional change in the acid environment of the compartment, identification of the ion channels involved in the response and, finally, the functional impact of the lack of Cl⁻ influx into the phagosomal lumen. To address these open questions, we have carried out investigations using live cell imaging to study phagosomal acidification, Cl⁻ content, and the molecular identity of the Cl⁻ permeability pathway in AMs during phagosomal acidification.

RESULTS

Chloride removal decreases phagosome acidification in murine alveolar macrophages

A correlative relationship has previously been observed between the intracellular concentration of Cl⁻ and acidification of a spectrum of intracellular vesicles including intact and isolated Golgi, endosomes and lysosomes, as well as phagosomes of granulocytes during particle uptake (Barasch and al-Awqati, 1993; Chakraborty et al., 2017; Painter and Wang, 2006; Sonawane et al., 2002) (Hara-Chikuma et al., 2005) (Wang, 2016). We postulated that acidification of phagosomes in alveolar macrophages (AMs) during maturation was dependent on intracellular Cl⁻ and driven by influx into the phagosomal lumen through anion channels. Cl⁻ transport serves as a charge shunt for the transport of protons into the phagosomal lumen by the electrogenic activity of the V-ATPase. We began our studies by simply examining phagosomal acidification in the presence and absence of external and internal Cl⁻. This required depletion of intracellular Cl⁻ in AMs before presenting them with cargo for phagocytic uptake. Previous studies focused on Cl⁻ regulation of intracellular processes have evaluated the depletion of intracellular Cl⁻ concentration as a function of a reduction in extracellular Cl⁻ concentration (Lambert and Lowe, 1978) (Butt et al., 1994) (Takeuchi et al., 1997) (Heimlich and Cidlowski, 2006). In our studies, cells were exposed to Cl⁻-depleted medium for >2 h to ensure maximum intracellular Cl⁻ depletion. Following phagocytic uptake of zymosan particles doubly conjugated to pH insensitive Rhodamine Green and the pH sensor pHrodo Red, time dependent changes in phagosomal acidification were imaged in live cell confocal microcopy (Figures 1A and 1B). As external particles labeled with the pH sensor were not visible in a neutral pH environment, the Rhodamine Green fluorescent signal was used to outline and track zymosan particles over time in 3D volume and the rendered voxels were used to measure changes in fluorescent intensities in the two channels. In addition to 3D tracking, traces lacking pH related changes in fluorescence intensities were excluded from analysis by applying an amplitude threshold filter (Figure 1C). Acidification profiles were compared in under control conditions and in cells maintained in Cl⁻-free media. The kinetics of acidification obtained after conversion of the dye ratio values to pH using the calibration curve (Figure 1D) are shown in Figure 1E. In Cl⁻-depleted cells, the level of phagosomal pH was significantly higher (0 mM Cl⁻, pH = 5.82 ± 0.24 at 24 min) than in cells maintained at control Cl⁻ levels (131.5 mM Cl⁻, pH = 4.78 ± 0.1 at 24 min). In order to examine the argument that the interplay between the inward flux of Cl⁻ and V-ATPase support phagosomal acidification, we performed immunofluorescence experiments staining for the lysosomal protein LAMP-1 at the 20 min point following zymosan uptake. The results of these experiments shown in Figure S1 demonstrated that lysosomal fusion occurs with phagosomes in experiments similar to those in Figure 1E in the presence and absence of Cl⁻. The *sine qua non* of phagosomal acidification is, however, acquisition and activation of the V-ATPase, as it is absent in experiments in the presence of the macrolide inhibitor of the pump, bafilomycin (BAF, 1 μM) even under control Cl⁻ conditions (Figure 1E).

Isolated phagosomal Cl permeability pathways: the digitonin model

Removal of Cl⁻ from the extracellular media tells us that Cl⁻ is an important mediator of acidification but it does not allow for the study of the concentration dependence of the response because we cannot
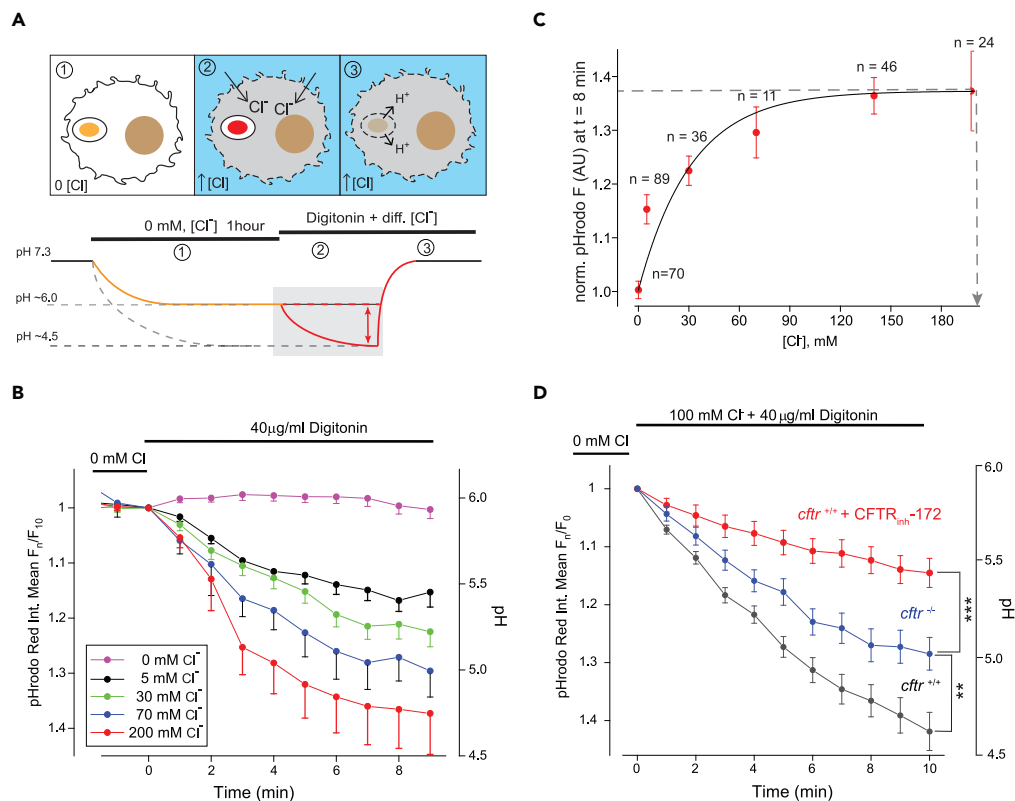
Figure 2. Intracellular chloride dependence of phagosomal acidification

(A) Cartoon depicting the sequence of the detergent assay for Cl^- concentration clamping during phagocytosis and phagosomal acidification. Upper panel, stages of detergent permeabilization of membranes and ion fluxes: 1) Zymosan phagocytosis in the absence of Cl^-, intact membranes, no detergent present. 2) Digitonin permeabilization of cell plasma membrane in the presence of Cl^- to load cytoplasm with the Cl^- concentration of interest. 3) Phagosomal membrane permeabilization with digitonin and that leads to its pH gradient disruption. Below, schematic diagram representing the time course of phagosomal acidification at different stages of membrane permeabilization with digitonin resulting in pHrodo Red fluorescence changes. Gray area indicates the period of intracellular phagosomal acidification measured after the addition of digitonin.

(B) The kinetics of normalized pHrodo Red fluorescence changes and corresponding phagosomal acidification after addition of 40 µg/mL digitonin in the presence of different Cl^- concentrations: 0 mM (n = 70 particles, 53 cells), 5 mM (n = 89 particles, 47 cells), 30 mM (n = 36 particles, 30 cells), 70 mM (n = 11 particles, 9 cells), 200 mM (n = 24 particles, 29 cells).

(C) Summary plot of the Cl^- concentration dependence of pHrodo Red fluorescence changes measured at 9 min following the addition of digitonin and at the indicated Cl^- concentration. The data was fitted with a dose-response curve with variable Hill slope function (y = A1+(A2-A1)/(1 + 10^((LOGx0-x)*p))) with maximum acidification reached at about 193 mM Cl^-.

(D) The kinetics of normalized pHrodo Red fluorescence changes and corresponding phagosomal acidification after addition of 40 µg/mL digitonin in the presence of 100 mM Cl^- in $cftr^{+/+}$ Control AMs (black trace, n = 117 particles, 72 cells); in $cftr^{-/-}$ AMs (blue trace, n = 89 particles, 66 cells) and in $cftr^{+/+}$ AMs in the presence of 10 µM CFTR$_{inh}$-172 (red trace, n = 100 particles, 61 cells). Data are represented as mean ± SEM. Significance levels determined by One-Way ANOVA Tukey test (**p<0.01, ***p<0.001).

control Cl^- concentrations on both sides of phagosomal membrane: intraluminal and cytoplasmic. This is best accomplished with an isolated phagosomal preparation. However, biochemical isolation of the organelle leaves membranes damaged resulting in leaky organelles. In order to avoid such permeability impairment, we utilized two techniques to study phagosomal Cl^- flux by either perforating or removing the plasma membrane barrier for solution access. The first technique involved gentle detergent permeabilization of the plasma membrane, thereby, allowing a Cl^- concentration clamp of the cytosolic ions surrounding the phagocytosed zymosan particles conjugated to the pH sensing dye pHrodo Red, as illustrated schematically in Figure 2A. Digitonin (40 µg/mL) works as a mild permeabilization agent that forms membrane pores enabling molecules like antibodies to pass without plasma membrane dissolution over a limited time period (Fiskum et al., 1980) (Miyamoto et al., 2008). Thus, our working assumption was that

it would provide enough time to achieve a cytosolic concentration clamp for highly mobile ions such as Cl^-.

Cultured AMs were exposed to the pH sensitive zymosan particles in a 0 mM Cl^- solution for an hour prior to cell exposure to permeabilizing digitonin solutions in order to achieve steady-state phagosomal acidification levels in the absence of Cl^-. Phagosomes loaded with pH sensitive cargo acidified to a moderate level in the cytoplasm that was depleted of Cl^- during the incubation period. At the end of the incubation period that allowed full depletion of cytoplasmic Cl^- as well as uptake of zymosan, cells were exposed to solutions of variable Cl^- concentrations containing 40 μg/mL digitonin (Figure 2B). In this manner, the cell cytoplasm could be clamped to a desired Cl^- concentration over a period of about 15–20 min before permeabilization spread to the phagosomal membrane detected by the subsequent rapid loss of phagosomal acidification. Stable new levels of phagosomal acidification could be reached over this time and increased as a function of increasing cytoplasmic Cl^- concentration. Only a single Cl^- concentration per experiment could be examined by this digitonin permeabilization protocol. Summarized mean peak acidification values (maximum pHrodo fluorescence at approximately 9 min of incubation) in different Cl^- concentrations are plotted in Figure 2C. The data was fitted with a dose-response curve with variable Hill slope function. Maximum levels of acidification were achieved at about 193 mM Cl^-. Previously published data from the laboratory indicated that the Cl^- channel, Cystic fibrosis transmembrane conductance regulator (CFTR) contributed to phagosomal membrane permeability (Di et al., 2006) (Deriy et al., 2009) (Riazanski et al., 2015). In Figure 2D, we compared the effect of genotype on acidification levels at a single intracellular Cl^- concentration with the digitonin permeabilization technique. Given the data correlating increases in cytoplasmic Cl^- with increases in phagosomal acidification in Figure 2B, we asked the question of whether loss of CFTR expression in AM phagosomes from genetically engineered $cftr^{-/-}$ mice or in AMs exposed to the specific CFTR inhibitor, CFTR$_{inh}$-172 (Figure 2D), show a comparative loss in acidification. The data from these experiments clearly correlates with decrements in cytoplasmic Cl^-. However, phagosomes from $cftr^{-/-}$ mice in colonies carried for years clearly appear to have developed an alternative shunt conductance pathway when compared to acidification levels seen in the phagosomes from the inhibitor-treated cells as documented in our earlier study demonstrating transgenic human CFTR mRNA present in AMs isolated from FABP hCFTR gut–corrected $cftr^{-/-}$ mice in an inbred colony (Deriy et al., 2009). The close correlation between phagosomes from cells treated with CFTR$_{inh}$-172 and $cftr^{-/-}$ with phagosomes from $cftr^{+/+}$ cells provided validation for the digitonin model and a saturation level for Cl^- and acidification levels within a single phagosome.

Isolated phagosomal Cl^- permeation in a microfluidics environment

The digitonin permeabilization model had the obvious drawback that Cl^- permeability could only be studied for one concentration in each experiment. The inevitable spread of digitonin permeabilization to the phagosomal membrane limited the study of multiple anion concentrations in a single preparation. Therefore, we transitioned our experiments to a microfluidics environment where single cells could be maintained for periods of up to nine days. When firmly attached to a glass substrate allowing confocal visualization, cells were exposed to and loaded with pH sensing zymosan and the entire chamber was transferred to a nitrogen cavitation device. Cells were disrupted exposing the isolated but still attached, fully functional phagosome. Solutions of increasing Cl^- concentration were superfused over a cell of interest in the microfluidics device positioned on the stage of a confocal microscope. Isolated, exposed phagosomes were identified visually as they contained a weakly fluorescent dye-conjugated zymosan particle. Phagosomes were identified as having intact membranes when they responded by an increase in fluorescence when exposed to a Cl^- containing solution seen schematically in Figure 3A. Peak fluorescence was reached over a period of approximately 5 min and was proportional to the Cl^- concentration as seen in Figure 3B. The response to an increase in extra-phagosomal Cl^- concentration was much faster than that seen in the digitonin permeabilization experiments of Figure 2. That was to be expected since solutions were perfused directly over the stabilized phagosome and did not have to diffuse through the permeabilized plasma membrane into the cell. When the peak fluorescence or acidification was plotted as a function of Cl^- (Figure 3C) the maximum levels of acidification were slightly lower than that seen in Figure 2 with the digitonin permeabilization model and achieved at about 188 mM Cl^-.

Quantitative measurement of phagosomal Cl^- in AMs from genetically engineered Cl^- channel knock out mice

In the preceding studies, we established the correlation between phagosomal acidification and cytosolic Cl^- by selective removal of the anion and replacement with the impermeant anion methanesulfonate

A

Phagocytosis in 0 mM Cl⁻

Cell membrane disruption

Imaging in different [Cl⁻]$_{out}$

Cell Culture on device

Nitrogen cavitation

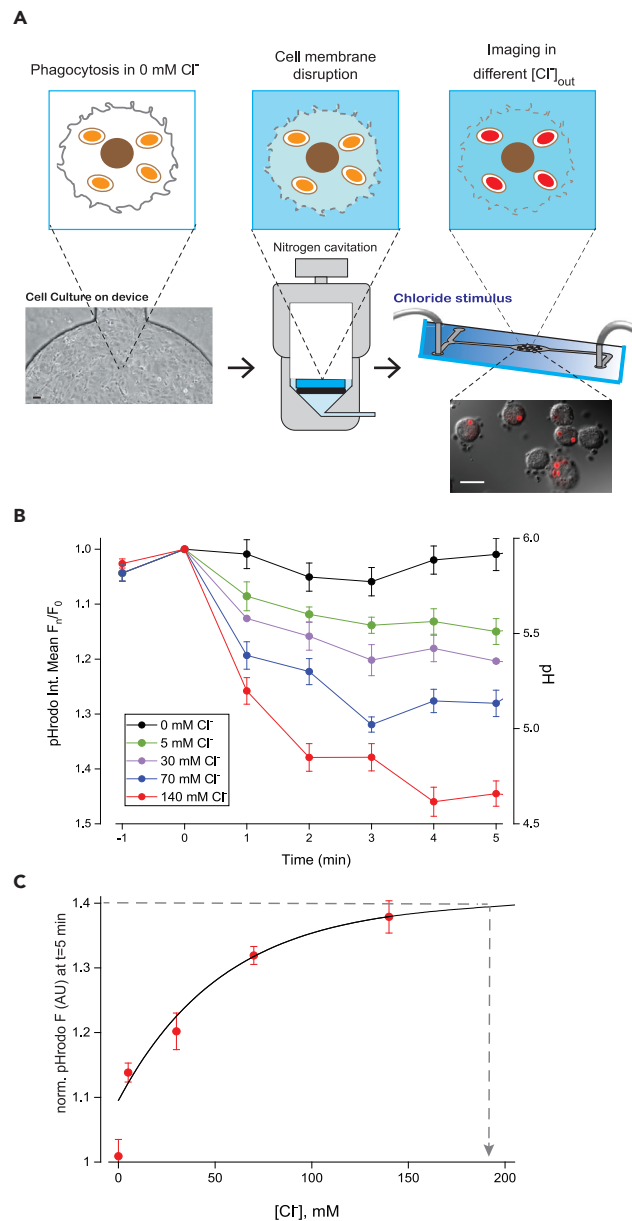Chloride stimulus

B

C

Figure 3. Phagosomal pH measurements on a microfluidic chip

(A) Schematic presentation of a time course experiment for the measurement of phagosomal pH changes. Cells are loaded and maintained in the chip before exposure to pHrodo Red conjugated zymosan particles. pHrodo Red is used to measure the changes in intraphagosomal pH. Nitrogen cavitation was used to permeabilize the cells within the microfluidic chip. Scale bars 20 μm.

(B) pH dependent fluorescent changes for pHrodo Red as the surrounding media is exchanged with different Cl⁻ concentrations. Cell membrane structure was disrupted via nitrogen cavitation allowing ion exchange within the phagosomes (140 mM: 3 chips, 17 cells, n = 49 individual phagosomes; 70 mM: 3 chips, 13 cells, n = 25 individual phagosomes; 30 mM: 4 chips, 13 cells, n = 39 individual phagosomes; 5 mM: 3 chips, 19 cells, n = 30 individual phagosomes; 0 mM: 3 chips, 28 cells, n = 48 individual phagosomes).

(C) Summary plot of pHrodo Red signal as a function of Cl⁻ concentration in the surrounding media measured at 5 min following the addition of the indicated Cl concentration. The data was fitted with a dose-response curve with variable Hill slope function (y = A1+(A2-A1)/(1 + 10^((LOGx0-x)*p))) with maximum acidification reached at about 188 mM Cl. A single chip represents an independent experiment. Data are represented as mean ± SEM.
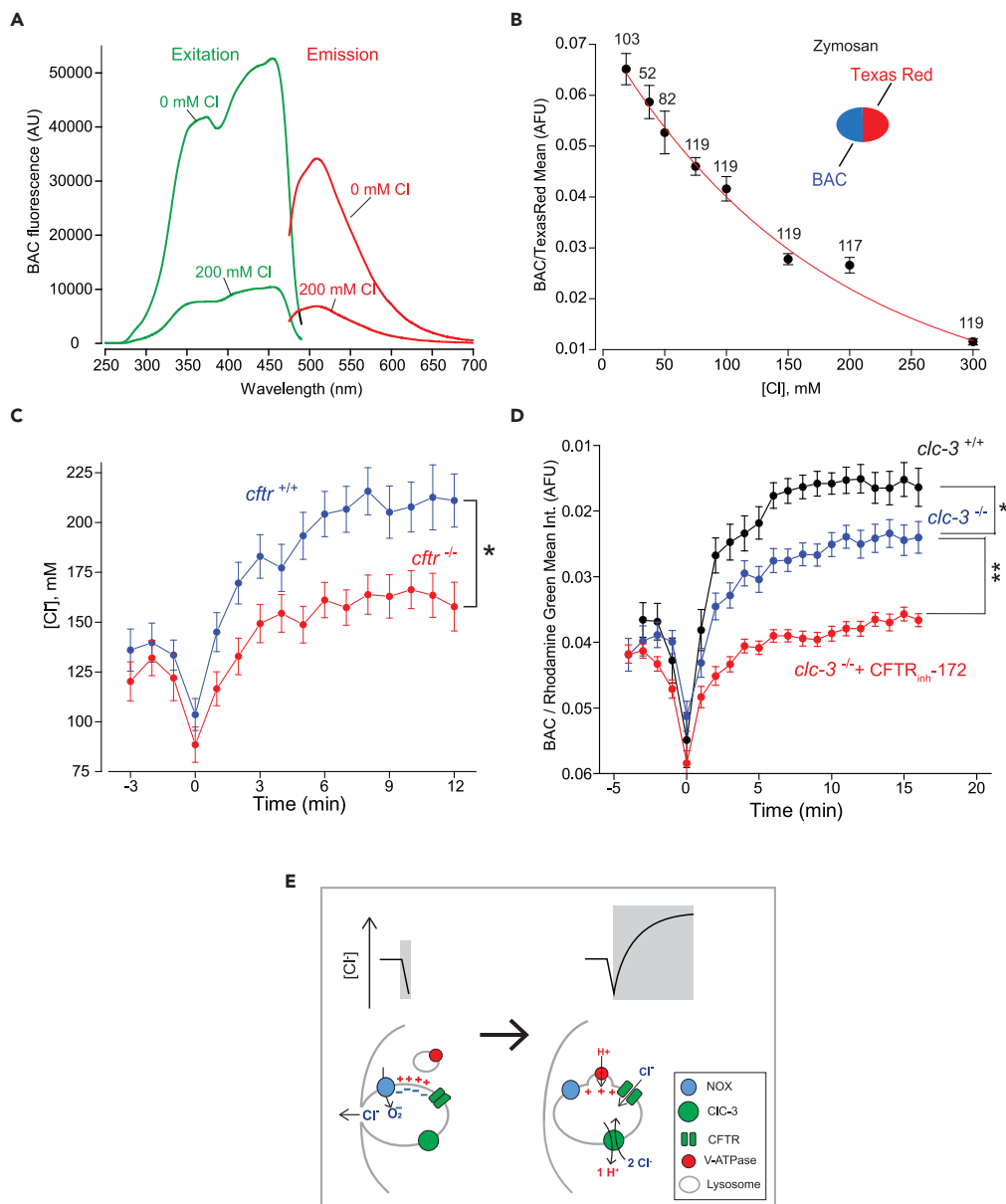
Figure 4. Phagosomal chloride concentration dynamics measured with BAC

(A) Spectral scans of BAC excitation (green) and emission (red) in the absence of Cl^- (0 mM Cl^-) and in 200 mM Cl^-.

(B) Chloride concentration dependent changes in BAC fluorescence normalized to Texas Red fluorescence. The averaged data points were fitted with exponential decay fit ($y = A1*exp(-x/t1)+y0$).

(C) Time course of phagosomal Cl^- concentration changes measured with BAC in $cftr^{+/+}$ Control (n = 67 particles, 43 cells) and in $cftr^{-/-}$ Control (n = 45 particles, 41 cells).

(D) Relative time course of BAC/Rhodamine Green mean fluorescence changes in $clc-3^{+/+}$ Control (black trace, n = 39 particles, 35 cells, 3 mice); in $clc-3^{-/-}$ Control (blue trace, n = 47 particles, 32 cells, 3 mice) and in $clc-3^{-/-}$ in the presence of 10 μM $CFTR_{inh}$-172 (red trace, n = 80 particles, 59 cells, 3 mice). Significance levels determined by One-Way ANOVA Tukey test: *$p<0.05$, **$p<0.01$.

(E) Schematic overview of phagosomal Cl^- concentration changes during early stages of phagolysosomal biogenesis. Electrogenic NOX activity started prior to phagosomal closure leads to O_2^- anion flux into the nascent phagosome, locally depolarizing the cellular membrane potential resulting from the associated proton/cation accumulation on the cellular cytoplasmic side and anion accumulation on the nascent phagosome luminal side. The superoxide anion accumulation

Figure 4. *Continued*
expels Cl⁻ anions from the interior of maturing phagosome through its closure. Following closure of the phagosome, phago-lysosomal fusion contributes V-ATPase proton pumps to the phagosomal membrane. V-ATPase activity increases proton influx into the phagosome, producing phagosomal acidification and depolarization (positive charge buildup) obligating Cl⁻ anion influx as a charge shunt. Data are represented as mean $\pm$ SEM.

($MeSO_4$) from the external media and, thereby, depleting Cl⁻ from the cytoplasm as well as from phago-somal lumen (Figure 1). Using phagosomal acidification as a surrogate reporter of phagosomal Cl⁻, we compared increasing acidification with increasing cytoplasmic Cl⁻ in two concentration-clamping models (Figures 2 and 3). The Cl⁻ concentration clamping models also allowed us to identify at least one of the molecular species of the Cl⁻ -influx pathway using both pharmacological and genetic approaches (Figure 2). In the next set of experiments, we estimated changes in intraphagosomal Cl⁻ following zymosan uptake using the Cl⁻ sensitive chromophore 10,10′-bis[3-carboxypropyl]-9,9′biacridinium dinitrate (BAC) conjugated to zymosan along with the Cl⁻ insensitive chromophore Texas Red used for particle tracking. BAC fluorescence decreases intensity with increasing Cl⁻ concentration and is insensitive to pH as has been shown previously (Sonawane et al., 2002). A wavelength scan of both excitation and emission of BAC as a function of Cl⁻ concentration is seen in Figure 4A. As noted by Sonawane et al. (Sonawane et al., 2002), BAC is highly sensitive to photobleaching. We have taken this into consideration and corrected changes in BAC fluorescence intensity for photobleaching during the imaging period. Following and calculating the decrease in BAC signal in zymosan particles remaining outside of the cells at corresponding time points allowed us to compensate for the BAC fluorescent signal amplitude decrease resulting from photobleaching. Low intensity illumination helped in this regard as well, but did not eliminate the problem. Chloride concentration dependency calibration of the doubly conjugated particles is plotted in Figure 4B. A comparison of dynamic changes in phagosomal Cl⁻ concentration in $cftr^{-/-}$ AMs versus cells from $cftr^{+/+}$ animals can be seen in Figure 4C. The maximum level of Cl⁻ in the $cftr^{+/+}$ phagosomes reaches 207 $\pm$ 11.5 mM and is similar to the maximum saturation values in the dose-response curves in Figures 2C and 3C. The $cftr^{-/-}$ cells exhibited a significantly lower intraphagosomal Cl⁻ level of 157 $\pm$ 8.8 mM. These data are consistent with the observation that CFTR represents a prominent influx pathway for Cl⁻ accumulation in the AM. The Cl⁻/H⁺ antiporter ClC-3 has been identified in endosomes in a number of cells including the macrophage cell line J774.1 (Sonawane et al., 2002) (Hara-Chikuma et al., 2005). The lyso-endosomal compartment fuses with the maturing phagosome and, therefore, would be expected to contribute to the spectrum of anion permeation pathways in the phagosome. We compared the magnitude of Cl⁻ uptake in phagosomes from wild type (clc-$3^{+/+}$) and clc-$3^{-/-}$ cells (Figure 4D) and there was a significant difference in the amount of phagosomal Cl⁻ change between two genotypes indicating that ClC-3 played a role, albeit a lessor role, in phagosomal Cl⁻ dynamics. Data from these experiments demonstrated that the anion channel CFTR was the major contributor to the anion charge-shunt pathway during phagosomal acidification providing the bulk of Cl⁻ accumulation.

Prominent in these studies was the immediate decrease in Cl⁻ concentration of the phagosomal lumen prior to the increase. It has been suggested that this is due to Donnan equilibrium effects in endosomes from the macrophage cell line J774 (Sonawane et al., 2002). Our recent data suggests that this transient loss of Cl⁻ is likely due to the influx of superoxide anions (O_2^-) into the phagosomal lumen providing a negative membrane potential during the activation of NADPH oxidase (NOX), which immediately precedes the onset of acidification. The influx of a negatively charged species would be expected to produce a phagosomal hyperpolarization, as described recently by Riazanski et al (Riazanski et al., 2020), thus supporting the efflux of Cl⁻ before full phagosomal closure. The transient phagosomal hyperpolarization would support the movement of Cl⁻ ions out of the phagosome prior to phagosomal closure as illustrated schematically in Figure 4E. The decrease in phagosomal Cl⁻ is transient and followed by an increase in Cl⁻ that reaches a maximum of about 200 mM in approximately 12 min, again consistent with the saturation value of phagosomal Cl⁻ determined in the experiments in Figures 2 and 3.

Comparative estimates of elemental phagosomal Cl in hard X-ray analytical experiments
Quantitative measurements of elemental Cl⁻ within the phagosome as a function of maturation, heretofore unknown, were made using X-ray fluorescence microscopy (XFM). XFM is a unique approach that can be used to map and probe native elemental content within a cell or organelle with a spatial resolution down to 30 nm without the need for dyes and their potential artifacts. A schematic of the experimental system is illustrated in Figure 5A. AMs were cultured on silicon nitride membrane windows before exposure to
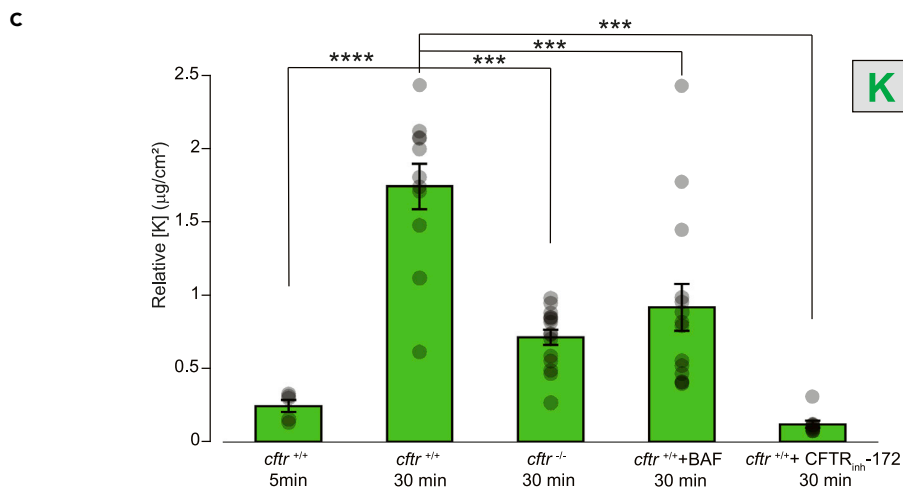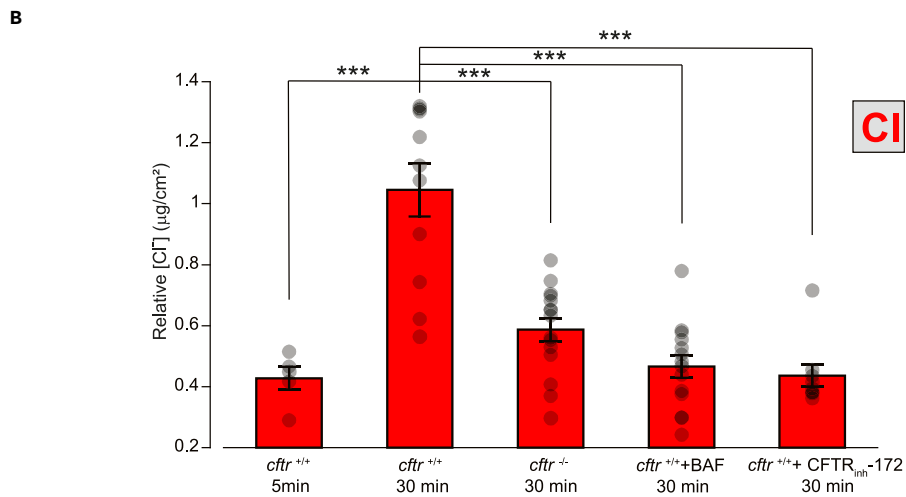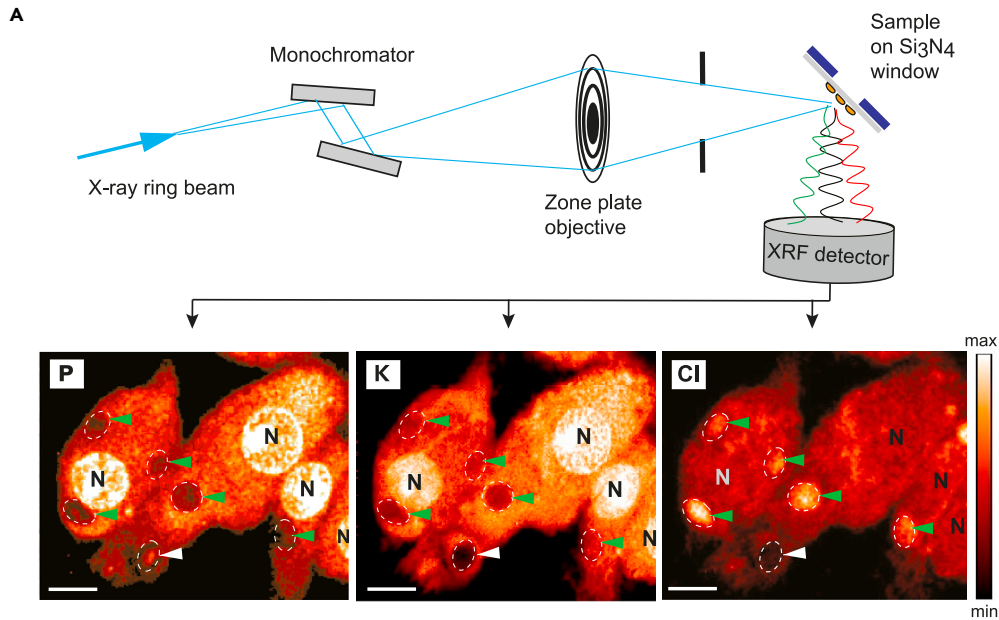
Figure 5. In-situ phagosomal chlorine measurements with X-ray spectroscopy

(A) Schematics of the Bionanoprobe - X-ray fluorescence nanoprobe for biological samples (adopted from Deng et al. (Deng et al., 2017)). A synchrotron generated, monochromatized X-ray beam is focused onto a sample using zone plate objective. Full spectra were acquired using an XRF detector while the sample is raster scanned forming 2D elemental maps for phosphorus (P), potassium (K) and chlorine (Cl) of same AMs with phagocytosed zymosan particles (arrows). Phagosomes can be identified by low signal levels in the phosphorus detection channel. Cell nuclei had a stronger phosphorus signal (N). An early phagosome had a lower chlorine signal (white arrow) than mature phagosomes (green arrows). Scale bar 5 μm.

(B) A summary plot of relative phagosomal chlorine concentrations presented as mean μg/cm^2: in Control $cftr^{+/+}$ macrophage samples frozen at 5 min after addition of zymosan to live AMs (0.417 ± 0.038 μg/cm^2, n = 5 phagosomes, 4 cells); in Control $cftr^{+/+}$ AM samples frozen at 30 min after addition of zymosan to live AMs (1.045 ± 0.087 μg/cm^2, n = 11 phagosomes, 6 cells); in $cftr^{-/-}$ macrophage samples frozen at 30 min after addition of zymosan to live macrophages (0.587 ± 0.038 μg/cm^2, n = 15 phagosomes, 5 cells); in $cftr^{+/+}$ macrophage samples frozen at 30 min after addition of zymosan to live macrophages in the presence of 1 μM BAF (0.466 ± 0.038 μg/cm^2, n = 14 phagosomes, 4 cells); in $cftr^{+/+}$ macrophage samples frozen at 30 min after addition of zymosan to live macrophages in the presence of 10 μM CFTR$_{inh}$-172 (0.436 ± 0.036 μg/cm^2, n = 9 phagosomes, 4 cells). Significance levels determined by One-Way ANOVA Tukey test (***p<0.001).

(C) A summary plot of relative phagosomal potassium concentrations presented as mean μg/cm^2: in Control $cftr^{+/+}$ macrophage samples frozen at 5 min after addition of zymosan to live AMs (0.246 ± 0.042 μg/cm^2, n = 5 phagosomes); in Control $cftr^{+/+}$ AM samples frozen at 30 min after addition of zymosan to live AMs (1.742 ± 0.155 μg/cm^2, n = 11 phagosomes); in $cftr^{-/-}$ macrophage samples frozen at 30 min after addition of zymosan to live macrophages (0.713 ± 0.052 μg/cm^2, n = 15 phagosomes); in $cftr^{+/+}$ macrophage samples frozen at 30 min after addition of zymosan to live macrophages in the presence of 1 μM BAF (0.917 ± 0.159 μg/cm^2, n = 14 phagosomes); in $cftr^{+/+}$ macrophage samples frozen at 30 min after addition of zymosan to live macrophages in the presence of 10 μM CFTR$_{inh}$-172 (0.121 ± 0.024 μg/cm^2, n = 9 phagosomes). Significance levels determined by One-Way ANOVA Tukey test (***p<0.001, ****p<0.0001). Data are represented as mean $\pm$ SEM.

and uptake of zymosan particles. Grids were plunge frozen at two time points, one at 5 min following the addition of zymosan in order to observe Cl$^-$ content at early times following phagosomal closure and another at 30 min following endo-lysosomal fusion. XFM images comparing elemental phosphorous (P), potassium (K), and chlorine (Cl) in the same set of phagosomes are illustrated in Figure 5A. Note elemental chlorine is annotated as Cl in the text as opposed to ionic chloride annotated as Cl$^-$. The magnitude of elemental content is depicted in a heat scale positioned to the right of the images and is not expressed as concentration but rather as a weight/volume measurement (see STAR Methods). Phosphorous is highest in the nucleus (N) and lowest in the phagosomes which are indicated by the green and white arrows. We used elemental P as an additional identifier in mapping phagosomes. The interior of phagosomes lacks extensive cytoplasmic phospholipid membrane and, therefore, appears as dark spotty areas of low P density in the projection images of phagosomal volume. Cl content was highest in the mature phagosomes and conversely lowest in cellular nuclei.

Comparative quantification of the elemental Cl data is summarized for both cell genotypes and pharmacological treatment in Figure 5B. Phagosomal Cl in mature phagosomes is compared in cells plunge frozen at 30 min following zymosan exposure, a time at which Cl$^-$ concentration was determined maximal (Figures 2,3, and 4). As seen in Figure 5B, Cl content at 30 min differed significantly in AMs from $cftr^{+/+}$ and $cftr^{-/-}$ mice as would be predicted from the BAC measurements of peak Cl content in Figure 4 comparing the two CFTR genotypes. Cells lacking the CFTR channel showed a significantly lower content as compared to $cftr^{+/+}$ cells. Cl content is driven by the activity of the vesicular ATPase. Cells exposed to the V-ATPase inhibitor bafilomycin (BAF) showed a significant decrease in Cl content as compared to control cells at 30 min. Cl content in BAF-treated cells was similar to content observed in $cftr^{+/+}$ cells in the presence of the CFTR$_{inh}$-172 inhibitor added prior to zymosan loading. Both conditions, blocking Cl$^-$ influx and blocking V-ATPase activity, resulted in a Cl content significantly decreased over that seen in wild type cells at the same time point.

K$^+$ content of phagosomes was of interest since K$^+$ movement out of the phagolysosome has been previously suggested to be an alternative charge-shunt pathway (Steinberg et al., 2010). This seemed unlikely as the concentration gradient for K$^+$, high K$^+$ in the cell (140 mM) and low K$^+$ in the phagosome, reflecting that in the extracellular solution (2.5 mM), and as such would predict a movement of K$^+$ into the phagosome. We examined the relative change in K content of phagosomes in the identical cells and, therefore, over the same time frame, cellular genetic source, and pharmacological modifiers of ion transport proteins tested in the Cl experiments in Figure 5B. As a significant experimental advantage, the XFM technique allows the
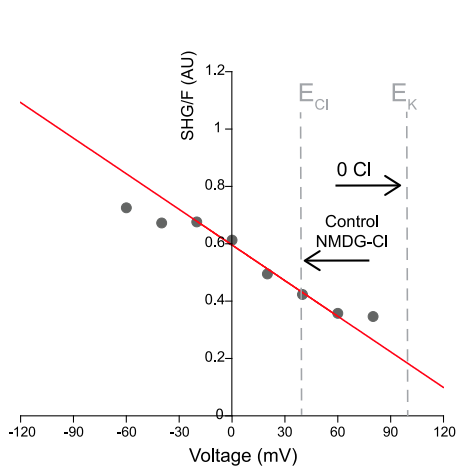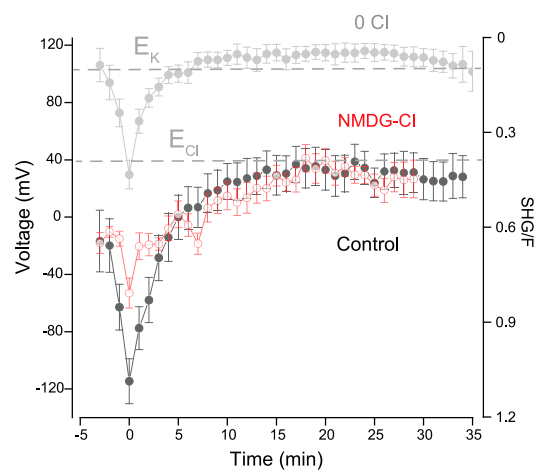
A
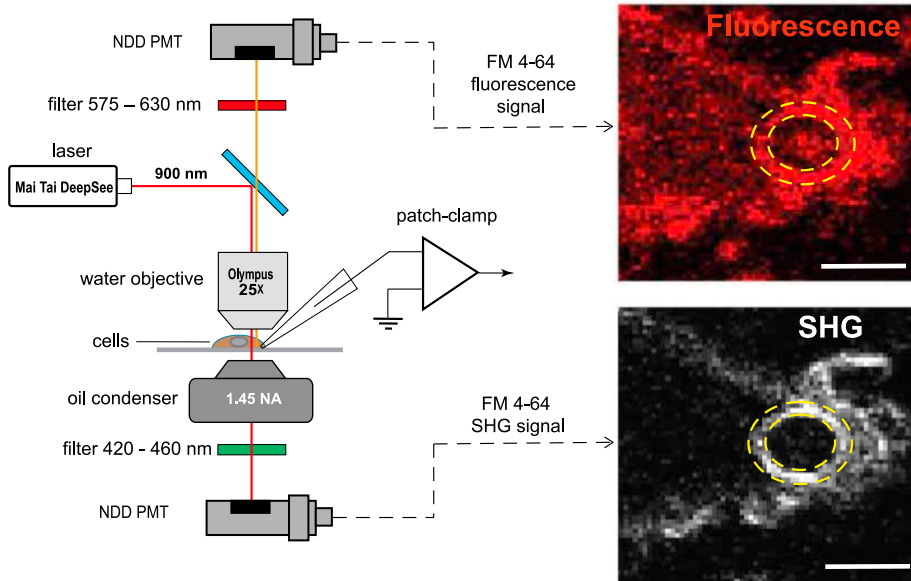
B
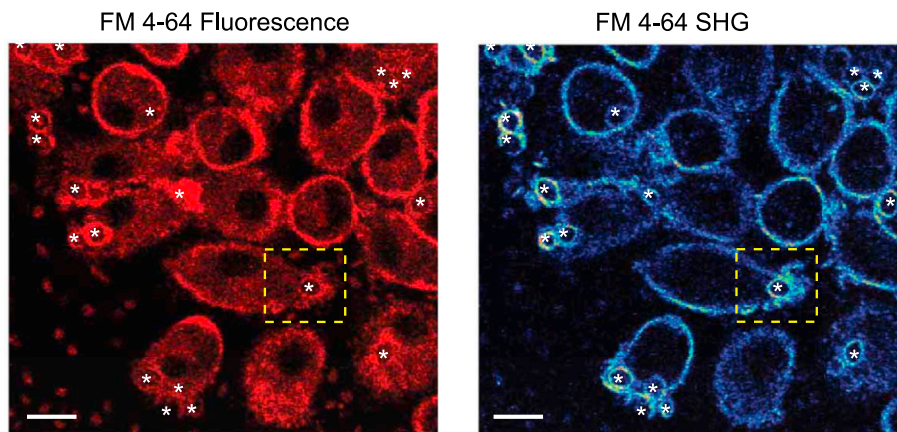
C

D

Figure 6. In-situ phagosomal voltage measurements with SHG microscopy

(A) A schematic presentation of combined SHG imaging and voltage-clamp patch-clamp recording setup. On the right: a representative confocal image section with a ring ROI (yellow) outlining phagosomal membrane for measurement of optical signal intensity in two channels: red – FM4-64 fluorescence; greyscale - FM4-64 SHG. Scale bars: 5 μm.

(B) A representative confocal cross-section image of *cftr*$^{+/+}$ macrophages obtained after labeling with 50 μM FM4-64 in two different channels: left (red pseudo color) – FM4-64 fluorescence image obtained with reflected NDD PMT after band pass emission filter of 575–630 nm; right (heat scale pseudo color) - FM4-64 SHG image obtained with a forward transmitted NDD PMT collected through a band-pass filter of 420 - 460 nm. Asterisks indicate locations of phagosomes at different stages of phagocytosis. Dashed line square – the section shown in (A) Scale bar – 10 μm.

(C) A representative normalized signal (SHG/F) to voltage (mV) correlation plot obtained with simultaneous whole-cell patch-clamp recordings and SHG imaging. The data were fitted with a line fit (red line, y = a+b*x).

(D) The time dependent changes in phagosomal voltage obtained after conversion of normalized (SHG/F) imaging signals from *cftr*$^{+/+}$ in Control ACSF (black circles, n = 24 phagosomes, 12 cells), from *cftr*$^{+/+}$ in 0 mM Cl$^-$ ACSF (gray circles, n = 10 phagosomes, 9 cells) and from J774 cells in NMDG-Cl ACSF (red hollow circles, n = 8 phagosomes, 8 cells). Data are represented as mean ± SEM.

acquisition of relative content measurements of multiple elements in the same structure, simultaneously. Thus, we were able to determine relative changes in K content in the same phagosomes that were examined in for relative changes in Cl content. Although we could not compare concentration changes directly, we could compare changes in content relative to a given element and compare those changes to a second element in the same phagosome. This comparison revealed that changes in Cl and K followed one another. In the presence of V-ATPase activity, the influx of Cl was mirrored as an influx or increase in K. This observation was initially somewhat counter intuitive. In the absence of V-ATPase activity, as in the presence of the inhibitor BAF, neither K nor Cl content increased relative to that seen at 30 min under control conditions. The absence of the Cl$^-$ channel CFTR or its inhibition by CFTR$_{inh}$-172 leads to a relative decrease in both K and Cl phagosomal content. The data suggested that it was the loss of the positive luminal potential produced by V-ATPase activity and the electrogenic influx of protons or the potential neutralization produced by the influx of Cl which allowed for the influx of K down its electrochemical gradient. Absent either one of those ion transport elements, the proton pump or the Cl$^-$ channels, K content did not increase. The determining factor in K movement is then the positive luminal voltage produced by the proton pump. If the anion channel is present it enhances the inward K driving force (Nernst equilibrium potential, E$_{K}$ = +100 mV) by reducing the positive luminal proton potential. If the proton pump is inhibited, the movement of anions will leave the phagosome down their concentration gradient of 200 mM phagosomal (see Figures 2 and 3) to 40 mM intracellular toward a positive Cl$^-$ equilibrium potential (Nernst equilibrium potential, E$_{Cl}$ = +40 mV). The movement of K ions into the phagosome will be limited by the positive equilibrium potential set by the Cl$^-$ conductance. If the Cl$^-$ influx is high, reducing the positive potential set by the proton pump, the influx of K$^+$ will increase in response to the gradient from 140 mM intracellular to 2.5 mM intraphagosomal. Thus, the organellar content of the two ions is limited and linked by membrane potential determined by the flow of ions down their respective electrochemical gradients and the driving force set by the activity of the proton pump.

Phagosomal membrane potential during zymosan uptake

The functional state of the phagosome is determined by membrane potential changes that determine the movement of channel-mediated ion fluxes across the organellar membrane. XFM has given us insight into the content of the phagosome taken from a snapshot in time. The dynamics of ion content is then determined by changes in membrane potential that integrate relative channel conductances rather randomly bestowed on the organelle during plasma membrane uptake and organellar fusion.

The final step in our investigation of Cl$^-$ dynamics in the phagosome was the determination of the time-dependent changes in membrane potential during phagocytic formation. We quantified membrane potential profiles in the phagosome in the presence and absence of Cl$^-$ during zymosan uptake. This we accomplished using the technique of second harmonic generation (SHG) imaging. The results of these studies are seen in Figure 6. Dynamic measurements of phagosomal membrane potential changes have not been reported, although a FRET-based approach reports a static (steady-state) membrane potential measurement of 28 mV lumen positive (Steinberg et al., 2007) with a very modest contribution of the V-ATPase to the membrane potential at steady-state of 14 mV. We examined the simultaneity of changes in phagosomal potential using SHG microscopy to measure membrane potential in developing phagosomes. The dye FM4-64 was loaded into cells that were illuminated with 1,064 nm/300-fs laser pulses to generate an intense

SHG signal from the labeled inner leaflet of the plasma membrane, as has been used in mammalian brain slices to measure membrane potentials in dendritic spines (Araya et al., 2006; Dombeck et al., 2005; Jiang et al., 2007; Jiang and Yuste, 2008; Nuriya et al., 2006). The elements of the signal acquisition and data analysis are depicted schematically in Figure 6A. Both the FM4-64 fluorescent signal and the SHG signal in macrophages in culture are compared in Figure 6B. Time dependent changes in these two signals allowed us to examine membrane potential changes in the nascent phagosome during the maturation process. In Figure 6D, changes in the ratio of the SHG signal to the fluorescence signal were converted to membrane potential in response to known voltage changes obtained in the whole-cell configuration of the patch-clamp technique. The patch clamp pipette measurement of membrane potential on single FM4-64 loaded cells is seen in Figure 6C. Voltage changes for calibration of the dye were made across a large voltage range; however, dye concentration changes seemed to be unavoidable leading to non-linearity at either end of the SHG/F-voltage curve over time and precluding repetitive measurements on the same cell (see Figure 6C). Thus, calibration of the dye ratio cannot be considered absolute but is rather a good approximation. Nonetheless, our voltage calibration data are in good agreement with those of Nuriya et al. (Nuriya et al., 2006) measured in dentritic spines where SHG is linear with voltage. Dynamic changes in phagosomal membrane potential following zymosan particle uptake are shown in Figure 6D under control conditions, in solutions in which the extracellular cations are replaced with the impermeant N-methyl glutamine (NMDG), and in solutions in which Cl^- has been replaced with the impermeant anion methanesulfonate. The membrane potential change was biphasic, hyperpolarizing upon entry of the phagosome into the cell due to the production of negatively charged free radicals contributing to the luminal negative charge (see schematic in Figure 4E) and the resultant transient loss of Cl^-. The maximum negative peak was followed by a luminal positive depolarization corresponding to the influx of Cl^- antagonizing the action of the rheogenic V-ATPase (see Figures 4C and 4D). Changes in pH as measured by pHrodo Red (increase in fluorescence with a decrease in pH) followed membrane potential as recently described by Riazanski et al (Riazanski et al., 2020). Dynamic changes in membrane potential (Figure 6D) in the presence of Cl^- (Control) and in the absence of extracellular permeant cations (NMDG-Cl) were not significantly different and were equal to E_{Cl} at steady state. When cells were incubated in solutions of lacking Cl^- (0 mM Cl^-) as in Figure 1, the steady-state phagosomal membrane potential was depolarized to and approximately equal to E_K. The movements of steady-state phagosomal membrane potentials under the three ionic conditions are indicated on the calibration curve in Figure 6C.

DISCUSSION

The link between CFTR and phagosomal Cl homeostasis and function: historical controversy

The genesis of our investigations determining the regulation of Cl-influx and acidification in AM phagosomes centered around the resolution of the controversy surrounding the question of the role of CFTR in phagosomal function. The link to the specialized Cl^- channel, CFTR, in AM biology came somewhat fortuitously from a quite unrelated direction. Our original observations, identifying CFTR as a major player in phagosomal acidification by AMs were driven by our observation that cultured AMs expressed a Cl^- selective current that was sensitive to cAMP levels introduced into the voltage clamped cell through the patch pipette as a putative seretagogue (Di et al., 2006). Cl^- channels had not been associated with phagocytic cell function to any significant degree. However, they had been implicated in the pH regulation of several organelles, presumably through the provision of counterions to neutralize lumenal H^+ accumulation (Hara-Chikuma et al., 2005). Our electrophysiological observation of CFTR in AMs became intriguing when we observed a link to AM function, namely bacterial killing. Previous studies identifying CFTR expression in the endosomal compartment led to the proposal that it may fulfill a counter-ion conductance role in this organelle (al-Awqati et al., 1992; Barasch and al-Awqati, 1993; Barasch et al., 1991; Chandy et al., 2001; Hara-Chikuma et al., 2005). Searching for a specific role for CFTR in AM biology, we determined that the loss of subcellular acidification in CFTR-deficient AMs was a key factor that contributed to the enhanced survival of bacterial loads within the phagosome and this loss of microbicidal function was related to CFTR genotype (Deriy et al., 2009). Simply put, CFTR in the phagosome of the AM appeared permissive for microbicidal function. While there remains disagreement over the acidification status of intracellular organelles in CF (Gibson et al., 2000; Hara-Chikuma et al., 2005; Luckie et al., 2001; Poschet et al., 2002), our data established the presence of CFTR in rodent and human AMs and suggested that CFTR played a significant role in macrophage organelle pH regulation. Initial contrasting opinions in the literature surrounding our phago-lysosomal observations emanated from two publications and focused on differences in the dye used to assay phagosomal pH, fluorescein versus Oregon Green, the genotype of the animals from which the AMs were obtained, $cftr^{-/-}$ versus ΔF508 and finally, the heterogeneity of phagosomal pH in a given AM population (Haggie and Verkman, 2007) (Steinberg et al.,

2010). It was tacitly agreed between the two camps that intracellular acidification in intracellular organelles, in general, is tightly linked to increases in Cl$^-$; however, the identity of the molecular pathway in each organelle met with much less agreement without firm substantiating data. Since that time, findings from Zhang et al. (Zhang et al., 2010) confirming our earlier data (Di et al., 2006) identify a population of secretory lysosomes which eventually fuse with phagosomes that exhibit a higher pH in *cftr*$^{-/-}$ AMs than in WT lung macrophages. The role of CFTR in bacterial clearance in the lung is further underscored in recent studies on CF pigs that develop human-like cystic fibrosis (CF) lung disease (Rogers et al., 2008a, 2008b, 2008c), however, the mechanism giving rise to pathogenesis may be quite different. Newborn pigs do not exhibit signs of airway inflammation but already display a defect in their ability to eliminate bacteria which leads to the accumulation of bacteria in the lungs (see review by Wine (Wine, 2010)). Data from Pezzulo et al. demonstrated that the pH of airway surface liquid was critical for rapid bacterial killing and its acidification in CF pigs led to reduced bacterial killing (Pezzulo et al., 2012) and not reduced bacterial killing by phagocytes resident in the pulmonary tree.

These studies further extend the question of whether rodent AM microbicidal dysfunction is a viable mechanistic model for chronic bacterial infections seen in CF. At issue is not the loss of function in phagocytic cells lacking CFTR but rather how the lack of CFTR controls defective bactericidal activity. One explanation is that failure of lysosomes and phagosomes to acidify properly due to the reduction of an anion influx mediated by CFTR. The severity of the acidification phenotype scales with the mutant genotype with ΔF508 being the most severe (Deriy et al., 2009). Phagocytosis *per se* is not affected and it does not appear that CFTR affects phago-lysosomal fusion or reactive oxygen species (ROS) production. However, in neutrophils lacking a functional CFTR, a concomitant defect in ROS generation due to a decrement in phagosomal Cl$^-$ has been suggested (Painter et al., 2006) (Painter et al., 2008) (Cifani et al., 2013) but remains controversial (Zhang et al., 2010) (McKeon et al., 2010).

In general, the molecular pathway mediating Cl$^-$ flux across organellar membranes is a subject of debate from phago-lysosomes to synaptic vesicles (Jentsch, 2007) (Jentsch, 2008) (Hubner and Jentsch, 2008) (Riazanski et al., 2011) (Ishida et al., 2013). Whether Cl channel species are unique to a given organellar type or could vary from one tissue type to another remains an open question. This is largely due to the lack of direct electrophysiological evidence quantifying differences in intraorganellar Cl$^-$ content/homeostasis as a function of Cl channel expression/identification and tissue type. However, the controversy surrounding the origin of the intracellular acidification defect in inflammatory cells in CF has been, to a large extent, resolved in experiments using myeloid Cftr-inactivated mice (Ng et al., 2014); CFTR expression is critical to normal host lung defense. While it is undisputed that the key substrate for production of the bactericidal HOCl in AMs and neutrophils is Cl$^-$, the details surrounding the dynamic regulation of intraphagosomal Cl$^-$ in the AM phagosome during the respiratory burst have been unexplored to date. Data in our current study provide direct evidence of the molecular species and the magnitude of the Cl$^-$ flux that accompanies particle uptake in pulmonary macrophages.

Our study addressed the over-arching question: How dependent is phagosomal acidification on Cl$^-$ and can we identify pathways for anion permeation in individual phagosomes during the endocytic process and the driving force that directs their movement? Our initial experiments explicating this question built on simply depleting cellular Cl$^-$ and demonstrated a 60% reduction in peak levels of acidification over a period of 20 min (Figure 1). In the digitonin permeabilization model in Figure 2D, we explored the impact of genotype on acidification carried out at a single Cl$^-$ concentration (100 mM). Pre-treatment of cells with the specific inhibitor of the Cl$^-$ channel CFTR in the same model also reduced peak acidfcation levels by approximately 69% (Figure 2D). These data confirmed earlier studies demonstrating that a significant fraction of phagosomal acidification was mediated by an influx of Cl$^-$ through the gating of CFTR as previously published (Di et al., 2006) (Radtke et al., 2011) (Riazanski et al., 2015). Surprisingly, however, acidification of phagosomes in AMs isolated from *cftr*$^{-/-}$ animals was only about 30% reduced over that observed in *cftr*$^{+/+}$. These data from genetically modified mice indicated that the *cftr*$^{-/-}$ animals maintained as a colony for an extended time likely developed an alternative conductance pathway for Cl$^-$ permeation. The alternative explanation, namely that the human CFTR expressed in the gut driven by the FABP promoter in these animals was no longer restricted to gut expression could not be ruled out and could account for the discrepancy between the data derived from pharmacological inhibition and that from the cells of *cftr*$^{-/-}$ animals. We have proffered this hypothesis for the discrepancy between genetic models and pharmacological inhibition in previous studies (Deriy et al., 2009).

The parameter triad determining degradative function in immune cell organelles

Our experiments were designed to study the phagosomal permeation of Cl^- in solutions in which Cl^- and K^+ were the significant permeant species. High K^+ solutions mimicked intracellular concentrations, with impermeant anion substitution for changing Cl^- concentrations. Solutions outside the cells during zymosan uptake and, therefore, inside the phagosome were extracellular in ionic composition with the exception of Cl^- as in the experiments in which extracellular (extra-phagosomal) Cl^- was varied by ionic substitution. Two different permeation models demonstrated a similar phagosomal Cl^- increase with acidification; luminal Cl^- scaling with increasing extra-phagosomal Cl^- concentration to maximal levels corresponding to maximum acidification reached at about 193 mM Cl^- (in Figure 2) and about 188 mM Cl^- (in Figure 3). These values are significantly higher than luminal Cl^- concentrations reported previously in endosomes from cultured J774.1 cells and lysosomes from *C. elegans* using BAC as a Cl^- sensor (Sonawane et al., 2002) (Chakraborty et al., 2017). These studies only examined changes in Cl^- over the linear range of the dye in compartments with a much smaller volume and dye concentration. Our estimates of Cl^- concentration at the initial stage of zymosan uptake before phagosomal closure (Figure 4C) approximated the Cl^- concentration in the extracellular solution of 140 mM and, therefore, validated our calibration technique.

It is important to note our XFM nanoprobe data give estimates of elemental chlorine and are not easily converted to values for concentrations of Cl^- ion. The values obtained in the nanoprobe experiments validate the comparable conditions and outcomes for the experiments in which concentrations of Cl^- were obtained and compared between genotypes and pharmacological treatments (see Figure 4). Data from the nanoprobe experiments show us that relative chlorine is significantly increased in phagosomes over 25 min of incubation, corresponding to end-stage phagosome maturation and the acquisition of transporters and channels following endo-lysosomal fusion. On the other hand, chlorine content is significantly decreased over control levels in $cftr^{-/-}$ cells, cells treated with the specific inhibitor $CFTR_{inh}$-172, and cells treated with BAF (1 μM). These data along with the data in Figures 1, 2, 3, and 4 provide strong evidence to show that Cl^- influx through CFTR contributes to accumulation of Cl^- within the phagosomal lumen in its charge neutralization role. XFM data in our experiments did present us with a mechanistic challenge. Relative changes in phagosomal K followed changes in chlorine content. We were not able to confirm the molecular identity of the influx pathway for K movement as the non-selective TRPML1 pathway derived from lysosomal fusion described by Samie et al. (Samie et al., 2013) and proposed for cation permeation in the endosomal compartment.

In our experiments, Na^+ was eliminated from the extracellular solutions leaving K^+ as the prominent permeant cation species. The driving force for K^+ movement out of the phagosome would require a large luminal positive voltage gradient to support an efflux of K^+ against a steep concentration gradient that would be needed to bring about charge neutralization and resultant luminal acidification in lysosomes as suggested in the data of Steinberg et al. (Steinberg et al., 2010). The modeling studies of Ishida et al. examining the ionic basis of lysosomal pH regulation concur with our observation (Ishida et al., 2013). Measurements of membrane potential correlated with phagosomal maturation were needed to provide the final answer to our observation of parallel changes in Cl^- and K^+ in the SHG experiments.

We, therefore, turned to ion substitution studies taking advantage of the technique of SHG using the fluorescent dye FM4-64 to monitor changes in phagosomal membrane potential over time following zymosan uptake under control conditions. We compared results under control conditions with data obtained in ion substitution experiments in the absence of Cl^- and in solutions in the absence of monovalent cations. A comparison of the three biophysical parameters controlling the dynamics of ion movement and phagosomal pH over time is illustrated in Figure 7 under initial conditions and at steady-state. Our data cannot identify the exact stage of phagosome closure, but suggest that the initiation of phagosomal membrane depolarization to a steady-state following a transient hyperpolarization, the decrease in pH to stable acidic levels following an alkalotic transient, and the initiation of the transient increase in Cl^- following the transient loss of Cl through the patent developing phagosome is consistent with plasma membrane closure as schematized in the gray box in Figure 7 as Stage 1. The fact that the influx of K^+ and Cl^+ are both driven by electrogenic V-ATPase activity is at first counter-intuitive; K^+ moving from a concentration gradient of high intracellular levels to lower phagosomal levels, and Cl^- moving from low intracellular levels to high phagosomal levels. The steady-state movement of both cations and the anions in response to the PMF is illustrated graphically within the gray box in Figure 7 as Stage 2. The link for passive, ion-channel mediated transport is driven off of and determined by the movement of protons and thereby, the
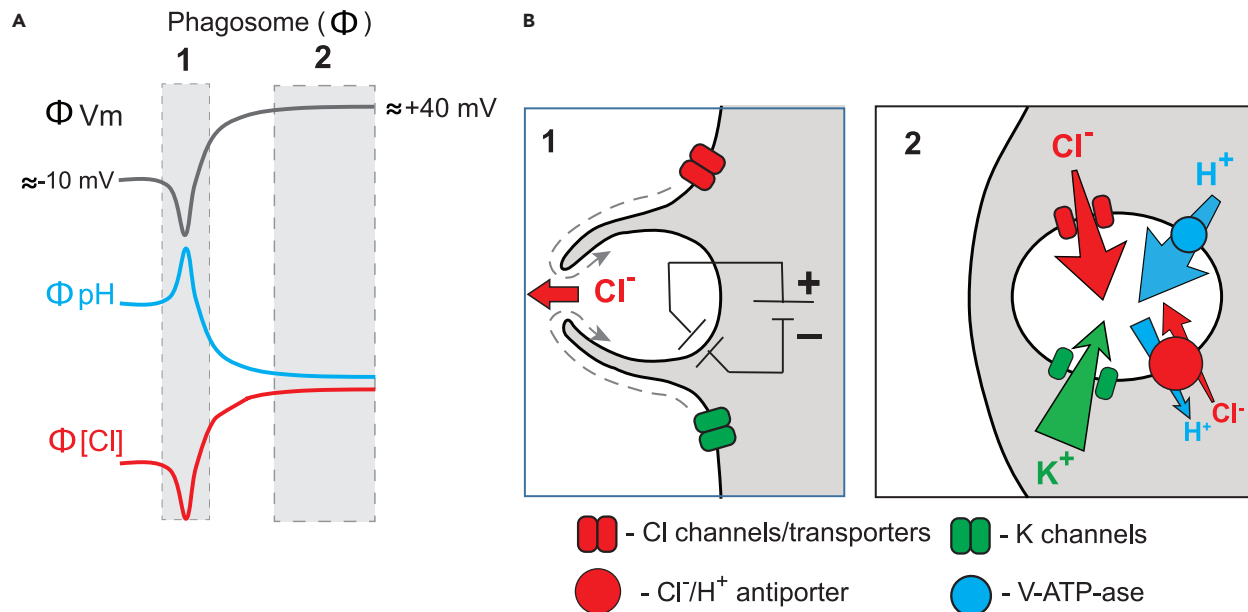
Figure 7. Biophysical changes during 2 stages of phagosome formation

(A) A schematic illustration of: phagosomal voltage change (gray line, Φ Vm), phagosomal pH change (blue line, Φ pH) and chloride concentration (red line, Φ [Cl]) inside of a phagosome during: 1) an initial phagosome formation, 2) steady-state levels during phagosomal maturation.

(B) Cartoons indicate directions of ion fluxes at the two phagosomal stages and identify polarity for voltage measurements.

membrane potential. If the proton motive force (PMF) is not compensated by Cl^-, then the phagosomal membrane potential will move to E_k. If Cl^- dependent charge neutralization is present, K^+ influx will occur and membrane potential will move to E_{Cl}.

It should be noted that the acquisition of transporters and channels in the phagosomal membrane is likely a function of nearest neighbors in the plasma membrane. As seen in schematic 1 in Figure 7B, Cl^- channels/transporters and K^+ channels are suggested to be moving from outside the phagosome to its interior. Given the tethering of CFTR to the cytoskeleton as described by Short et al. (Short et al., 1998) there is a strong possibility that channels and transporters within the region of membrane that forms the phagosome are thereby internalized as bystanders.

Multi-parameter determinant of phagosomal function

In summary, we have shown that Cl^- levels in mature phagosomes in AMs are contributed to and controlled by the anion channel CFTR. The Cl^-/H^+ antiporter ClC-3 contributed by endosomal/lysosomal fusion appears to have a negligible effect on phagosomal Cl^- dynamics. The intraluminal influx of Cl^- is correlated with organellar acidification reaching a maximum within 10 min after particle uptake. Levels of Cl^- in the mature phagosome are higher than previously reported, are approximately 190–200 mM, and may contribute to the activity of degradative enzymes independent of pH. Phagocytes lacking CFTR expression and, therefore, the crucial charge shunt permissive for acidification and concomitantly bacterial killing, likely contribute to defects in both oxidative and non-oxidative microbicidal pathways in CF.

Limitations of the study

We limited our study of phagosomal chloride homeostasis to activity in pulmonary AMs. Biological variability, in the comparative analysis of our study, will and does involve macrophage tissue source since acquisition of Cl^- selective influx pathways is stochastic and dependent upon plasma membrane channel expression. Our choice of pulmonary macrophages allowed us to examine the dynamics of Cl^- homeostasis and its impact on the maintenance of luminal pH using methods well-developed in our laboratory for this preparation including fluorescent dyes and high resolution live cell microscopic techniques (Di et al., 2006) (Deriy et al., 2009) (Riazanski et al., 2015). We have drawn AMs exclusively from rodent sources recognizing the possibility that expression of human CFTR expression driven by the FABP promoter designed to be

confined to the gut in the *cftr*$^{-/-}$ animal may have drifted to the lung with age of the mouse colony. This possibility would lead to a larger than predicted phagosomal Cl^- influx in cells from *cftr*$^{-/-}$ animals. Comparisons to human AMs were limited by the fact that BAL procedures are contraindicated in the routine clinical care of CF pediatric patients and only rarely available in adult CF patients. BAL, the source of human AMs in the general patient population, was not available in the current Covid pandemic environment. The use of the small molecule CFTRinh-172 as a surrogate for the *cftr*$-/-$ cells has reported limitations. Although CFTRinh-172 is the best available CFTR inhibitor, it is not specific as reported in the recent literature. It is reported to inhibit mitochondrial function and volume-regulated Cl-currents (Kelly et al., 2010) (Melis et al., 2014).

Although our experimental emphasis has been on the physiology of AMs, our approach could certainly be extended to other phagocytic tissue macrophages that express CFTR including peritoneal macrophages (see data comparing acidification in AMs and peritoneal macrophages in Figure S2) and generalized to other phagocytic cell lines in including microglial BV2/SMA9 or RAW cells which are adherent. The prevailing pH of the phagosome is no doubt determined to the greatest extent by the electrogenic proton pump, the activity of which is supported and maintained by the complex interplay of ion channels that provide counter-ion permeation pathways and transporters that provide proton leak pathways, including the solute carrier group of membrane transport proteins. These are collectively contributed by endocytic fusion with the maturing phagosome and are derived from plasma membrane sources during cargo uptake. This process is decidedly not a deterministic process and therefore contributes to the pH variability between phagosomes in a single cell. Dependence upon fluorescent ion sensitive dyes conjugated to cargo lends a large degree of variability, as each conjugation with multiple dyes is distinct with respect to dye stoichiometry and must be calibrated in each experiment, and a single conjugation batch needs to be used in experiments comparing genotype and pharmacological treatment.

STAR★METHODS

Detailed methods are provided in the online version of this paper and include the following:

- KEY RESOURCES TABLE
- RESOURCE AVAILABILITY
  - Lead contact
  - Materials availability
  - Data and code availability
- EXPERIMENTAL MODEL AND SUBJECT DETAILS
  - Cell lines
  - Origin and source of the animal
  - Ethical approval
  - Animal handling
  - Anesthetic protocols and euthanasia
- METHOD DETAILS
  - Bronchoalveolar lavage from mice
  - Live cell time-lapse imaging
  - Second-harmonics generation (SHG) imaging
  - SHG image analysis
  - Electrophysiology
- QUANTIFICATION AND STATISTICAL ANALYSIS

SUPPLEMENTAL INFORMATION

Supplemental information can be found online at https://doi.org/10.1016/j.isci.2021.103636.

AUTHOR CONTRIBUTIONS

Conception and design of the research: V.R., G.M., S.C., and, D.J.N. Performed the experiments: V.R., G.M. A.Z. and S.C. Performed the analyses: V.R., G.M. and S.C. Interpreted the results: V.R., G.M., D.J.N. and S.C. Drafted the manuscript: V.R. and D.J.N. Edited and revised the manuscript: All authors. All read and approved the final version. D.J.N. is the guarantor of this work and, as such, had full access to all the data in the study and takes responsibility for the integrity of the data and the accuracy of the data analysis.

DECLARATION OF INTERESTS

The authors declare no competing interests.

REFERENCES

al-Awqati, Q., Barasch, J., and Landry, D. (1992). Chloride channels of intracellular organelles and their potential role in cystic fibrosis. J. Exp. Biol. *172*, 245–266.

Araya, R., Jiang, J., Eisenthal, K.B., and Yuste, R. (2006). The spine neck filters membrane potentials. Proc. Natl. Acad. Sci. U S A *103*, 17961–17966.

Barasch, J., and al-Awqati, Q. (1993). Defective acidification of the biosynthetic pathway in cystic fibrosis. J.Cell Sci. Suppl. *17*, 229–233.

Barasch, J., Kiss, B., Prince, A., Saiman, L., Gruenert, d., and Al-Awqati, Q. (1991). Defective acidification of intracellular organelles in cystic fibrosis. Nature *352*, 70–73.

Butt, A.G., McLaughlin, C.W., Bowler, J.M., Purves, R.D., and Macknight, A.D. (1994). Cell Cl and transepithelial na transport in toad urinary bladder. J. Membr. Biol. *142*, 9–20.

Chadwick, S.R., Grinstein, S., and Freeman, S.A. (2021). From the inside out: ion fluxes at the centre of endocytic traffic. Curr. Opin.Cell Biol. *71*, 77–86.

Chakraborty, K., Leung, K., and Krishnan, Y. (2017). High lumenal chloride in the lysosome is critical for lysosome function. Elife *6*, e28862.

Chandy, G., Grabe, M., Moore, H.P., and Machen, T.E. (2001). Proton leak and CFTR in regulation of Golgi pH in respiratory epithelial cells. Am. J. Physiol. *281*, C908–C921.

Chen, S., Paunesku, T., Yuan, Y., Jin, Q., Hornberger, B., Flachenecker, C., Lai, B., Brister, K., Jacobsen, C., Woloschak, G., et al. (2015). The bionanoprobe: synchrotron-based

hard X-ray fluorescence microscopy for 2D/3D trace element mapping. Micros. Today *23*, 26–29.

Chen, C.C., Cang, C., Fenske, S., Butz, E., Chao, Y.K., Biel, M., Ren, D., Wahl-Schott, C., and Grimm, C. (2017). Patch-clamp technique to characterize ion channels in enlarged individual endolysosomes. Nat. Protoc. *12*, 1639–1658.

Cifani, N., Pompili, B., Anile, M., Patella, M., Diso, D., Venuta, F., Cimino, G., Quattrucci, S., Di Domenico, E.G., Ascenzioni, F., et al. (2013). Reactive-oxygen-species-mediated P. aeruginosa killing is functional in human cystic fibrosis macrophages. PLoS One *8*, e71717.

Deng, J., Vine, D.J., Chen, S., Jin, Q., Nashed, Y.S., Peterka, T., Vogt, S., and Jacobsen, C. (2017). X-ray ptychographic and fluorescence microscopy of frozen-hydrated cells using continuous scanning. Sci. Rep. *7*, 445.

Deriy, L.V., Gomez, E.A., Zhang, G., Beacham, D.W., Hopson, J.A., Gallan, A.J., Shevchenko, P.D., Bindokas, V.P., and Nelson, D.J. (2009). Disease-causing mutations in the cystic fibrosis transmembrane conductance regulator determine the functional responses of alveolar macrophages. J. Biol. Chem. *284*, 35926–35938.

Di, A., Brown, M.E., Deriy, L.V., Li, C., Szeto, F.L., Chen, Y., Huang, P., Tong, J., Naren, A.P., Bindokas, V., et al. (2006). CFTR regulates phagosome acidification in macrophages and alters bactericidal activity. Nat.Cell Biol. *8*, 933–944.

Dickerson, L.W., Bonthius, D.J., Schutte, B.C., Yang, B., Barna, T.J., Bailey, M.C., Nehrke, K., Williamson, R.A., and Lamb, F.S.

(2002). Altered GABAergic function accompanies hippocampal degeneration in mice lacking ClC-3 voltage-gated chloride channels. Brain Res. *958*, 227–250.

Dombeck, D.A., Sacconi, L., Blanchard-Desce, M., and Webb, W.W. (2005). Optical recording of fast neuronal membrane potential transients in acute mammalian brain slices by second-harmonic generation microscopy. J. Neurophysiol. *94*, 3628–3636.

Dong, X.P., Cheng, X., Mills, E., Delling, M., Wang, F., Kurz, T., and Xu, H. (2008). The type IV mucolipidosis-associated protein TRPML1 is an endolysosomal iron release channel. Nature *455*, 992–996.

Fiskum, G., Craig, S.W., Decker, G.L., and Lehninger, A.L. (1980). The cytoskeleton of digitonin-treated rat hepatocytes. Proc. Natl. Acad. Sci. U S A *77*, 3430–3434.

Gibson, G.A., Hill, W.G., and Weisz, O.A. (2000). Evidence against the acidification hypothesis in cystic fibrosis. Am. J. Physiol. *279*, C1088–C1099.

Hackam, D.J., Rotstein, O.D., Zhang, W.J., Demaurex, N., Woodside, M., Tsai, O., and Grinstein, S. (1997). Regulation of phagosomal acidification. Differential targeting of Na+/H+ exchangers, Na+/K+-ATPases, and vacuolar-type H+-atpases. J. Biol. Chem. *272*, 29810–29820.

Haggie, P.M., and Verkman, A.S. (2007). Cystic fibrosis transmembrane conductance regulator-independent phagosomal acidification in macrophages. J. Biol. Chem. *282*, 31422–31428.

Hara-Chikuma, M., Yang, B., Sonawane, N.D., Sasaki, S., Uchida, S., and Verkman, A.S. (2005). ClC-3 chloride channels facilitate endosomal

acidification and chloride accumulation. J. Biol. Chem. *280*, 1241–1247.

Heimlich, G., and Cidlowski, J.A. (2006). Selective role of intracellular chloride in the regulation of the intrinsic but not extrinsic pathway of apoptosis in Jurkat T-cells. J. Biol. Chem. *281*, 2232–2241.

Hubner, C.A., and Jentsch, T.J. (2008). Channelopathies of transepithelial transport and vesicular function. Adv. Genet. *63*, 113–152.

Ishida, Y., Nayak, S., Mindell, J.A., and Grabe, M. (2013). A model of lysosomal pH regulation. J. Gen. Physiol. *141*, 705–720.

Jentsch, T.J. (2007). Chloride and the endosomal-lysosomal pathway: emerging roles of CLC chloride transporters. J. Physiol. *578*, 633–640.

Jentsch, T.J. (2008). CLC chloride channels and transporters: from genes to protein structure, pathology and physiology. Crit. Rev. Biochem. Mol. Biol. *43*, 3–36.

Jentsch, T.J., and Pusch, M. (2018). CLC chloride channels and transporters: structure, function, physiology, and disease. Physiol. Rev. *98*, 1493–1590.

Jiang, J., and Yuste, R. (2008). Second-harmonic generation imaging of membrane potential with photon counting. Microsc. Microanal. *14*, 526–531.

Jiang, J., Eisenthal, K.B., and Yuste, R. (2007). Second harmonic generation in neurons: electro-optic mechanism of membrane potential sensitivity. Biophys. J. *93*, L26–L28.

Kelly, M., Trudel, S., Brouillard, F., Bouillaud, F., Colas, J., Nguyen-Khoa, T., Ollero, M., Edelman, A., and Fritsch, J. (2010). Cystic fibrosis transmembrane regulator inhibitors CFTR(inh)-172 and GlyH-101 target mitochondrial functions, independently of chloride channel inhibition. J. Pharmacol. Exp. Ther. *333*, 60–69.

Lambert, A., and Lowe, A.G. (1978). Chloride/bicarbonate exchange in human erythrocytes. J. Physiol. *275*, 51–63.

Luckie, D.B., Singh, C.N., Wine, J.J., and Wilterding, J.H. (2001). CFTR activation raises extracellular pH of NIH/3T3 mouse fibroblasts and C127 epithelial cells. J. Membr. Biol. *179*, 275–284.

McKeon, D.J., Cadwallader, K.A., Idris, S., Cowburn, A.S., Pasteur, M.C., Barker, H., Haworth, C.S., Bilton, D., Chilvers, E.R., and Condliffe, A.M. (2010). Cystic fibrosis neutrophils have normal intrinsic reactive oxygen species generation. Eur. Respir. J. *35*, 1264–1272.

Melis, N., Tauc, M., Cougnon, M., Bendahhou, S., Giuliano, S., Rubera, I., and Duranton, C. (2014). Revisiting CFTR inhibition: a comparative study of CFTRinh -172 and GlyH-101 inhibitors. Br. J. Pharmacol. *171*, 3716–3727.

Mindell, J.A. (2012). Lysosomal acidification mechanisms. Annu. Rev. Physiol. *74*, 69–86.

Miyamoto, K., Yamashita, T., Tsukiyama, T., Kitamura, N., Minami, N., Yamada, M., and Imai, H. (2008). Reversible membrane permeabilization of mammalian cells treated with digitonin and its use for inducing nuclear reprogramming by Xenopus egg extracts. Cloning Stem Cells *10*, 535–542.

Ng, H.P., Zhou, Y., Song, K., Hodges, C.A., Drumm, M.L., and Wang, G. (2014). Neutrophil-mediated phagocytic host defense defect in myeloid Cftr-inactivated mice. PLoS One *9*, e106813.

Nuriya, M., Jiang, J., Nemet, B., Eisenthal, K.B., and Yuste, R. (2006). Imaging membrane potential in dendritic spines. Proc. Natl. Acad. Sci. U S A *103*, 786–790.

Painter, R.G., and Wang, G. (2006). Direct measurement of free chloride concentrations in the phagolysosomes of human neutrophils. Anal. Chem. *78*, 3133–3137.

Painter, R.G., Valentine, V.G., Lanson, N.A., Jr., Leidal, K., Zhang, Q., Lombard, G., Thompson, C., Viswanathan, A., Nauseef, W.M., Wang, G., et al. (2006). CFTR Expression in human neutrophils and the phagolysosomal chlorination defect in cystic fibrosis. Biochemistry *45*, 10260–10269.

Painter, R.G., Bonvillain, R.W., Valentine, V.G., Lombard, G.A., LaPlace, S.G., Nauseef, W.M., and Wang, G. (2008). The role of chloride anion and CFTR in killing of Pseudomonas aeruginosa by normal and CF neutrophils. J. Leukoc. Biol. *83*, 1345–1353.

Pezzulo, A.A., Tang, X.X., Hoegger, M.J., Abou Alaiwa, M.H., Ramachandran, S., Moninger, T.O., Karp, P.H., Wohlford-Lenane, C.L., Haagsman, H.P., van Eijk, M., et al. (2012). Reduced airway surface pH impairs bacterial killing in the porcine cystic fibrosis lung. Nature *487*, 109–113.

Poschet, J., Perkett, E., and Deretic, V. (2002). Hyperacidification in cystic fibrosis: links with lung disease and new prospects for treatment. Trends Mol. Med. *8*, 512–519.

Radtke, A.L., Anderson, K.L., Davis, M.J., DiMagno, M.J., Swanson, J.A., and O'Riordan, M.X. (2011). Listeria monocytogenes exploits cystic fibrosis transmembrane conductance regulator (CFTR) to escape the phagosome. Proc. Natl. Acad. Sci. U S A *108*, 1633–1638.

Riazanski, V., Deriy, L.V., Shevchenko, P.D., Le, B., Gomez, E.A., and Nelson, D.J. (2011). Presynaptic CLC-3 determines quantal size of inhibitory transmission in the hippocampus. Nat. Neurosci. *14*, 487–494.

Riazanski, V., Gabdoulkhakova, A.G., Boynton, L.S., Eguchi, R.R., Deriy, L.V., Hogarth, D.K., Loaec, N., Oumata, N., Galons, H., Brown, M.E., et al. (2015). TRPC6 channel translocation into phagosomal membrane augments phagosomal function. Proc. Natl. Acad. Sci. U S A *112*, E6486–E6495.

Riazanski, V., Sui, Z., and Nelson, D.J. (2020). Kinetic separation of oxidative and non-oxidative metabolism in single phagosomes from alveolar macrophages: impact on bacterial killing. iScience *23*, 101759.

Rogers, C.S., Abraham, W.M., Brogden, K.A., Engelhardt, J.F., Fisher, J.T., McCray, P.B., Jr., McLennan, G., Meyerholz, D.K., Namati, E., Ostedgaard, L.S., et al. (2008a). The porcine lung as a potential model for cystic fibrosis. Am. J. Physiol. Lung Cell. Mol. Physiol. *295*, L240–L263.

Rogers, C.S., Hao, Y., Rokhlina, T., Samuel, M., Stoltz, D.A., Li, Y., Petroff, E., Vermeer, D.W., Kabel, A.C., Yan, Z., et al. (2008b). Production of CFTR-null and CFTR-DeltaF508 heterozygous pigs by adeno-associated virus-mediated gene targeting and somatic cell nuclear transfer. J. Clin.Invest. *118*, 1571–1577.

Rogers, C.S., Stoltz, D.A., Meyerholz, D.K., Ostedgaard, L.S., Rokhlina, T., Taft, P.J., Rogan, M.P., Pezzulo, A.A., Karp, P.H., Itani, O.A., et al. (2008c). Disruption of the CFTR gene produces a model of cystic fibrosis in newborn pigs. Science *321*, 1837–1841.

Samie, M., Wang, X., Zhang, X., Goschka, A., Li, X., Cheng, X., Gregg, E., Azar, M., Zhuo, Y., Garrity, A.G., et al. (2013). A TRP channel in the lysosome regulates large particle phagocytosis via focal exocytosis. Dev.Cell *26*, 511–524.

Short, D.B., Trotter, K.W., Reczek, D., Kreda, S.M., Bretscher, A., Boucher, R.C., Stutts, M.J., and Milgram, S.L. (1998). An apical PDZ protein anchors the cystic fibrosis transmembrane conductance regulator to the cytoskeleton. J. Biol. Chem. *273*, 19797–19801.

Skelley, A.M., Kirak, O., Suh, H., Jaenisch, R., and Voldman, J. (2009). Microfluidic control of cell pairing and fusion. Nat. Methods *6*, 147–152.

Sonawane, N.D., Thiagarajah, J.R., and Verkman, A.S. (2002). Chloride concentration in endosomes measured using a ratioable fluorescent Cl-indicator: evidence for chloride accumulation during acidification. J. Biol. Chem. *277*, 5506–5513.

Steinberg, B.E., Touret, N., Vargas-Caballero, M., and Grinstein, S. (2007). In situ measurement of the electrical potential across the phagosomal membrane using FRET and its contribution to the proton-motive force. Proc. Natl. Acad. Sci. U S A *104*, 9523–9528.

Steinberg, B.E., Huynh, K.K., Brodovitch, A., Jabs, S., Stauber, T., Jentsch, S., and Grinstein, S. (2010). A cation counterflux supports lysosomal acidification. J.Cell Biol. *189*, 1171–1186.

Takeuchi, S., Ando, M., and Irimajiri, A. (1997). Changes in the volume of marginal cells induced by isotonic 'Cl- depletion/restoration': involvement of the Cl- channel and Na+-K+-Cl- cotransporter. Hear. Res. *113*, 99–109.

Twining, B.S., Baines, S.B., Fisher, N.S., Maser, J., Vogt, S., Jacobsen, C., Tovar-Sanchez, A., and Sanudo-Wilhelmy, S.A. (2003). Quantifying trace elements in individual aquatic protist cells with a synchrotron X-ray fluorescence microprobe. Anal. Chem. *75*, 3806–3816.

van Heeckeren, A.M., Schluchter, M.D., Drumm, M.L., and Davis, P.B. (2004). Role of Cftr genotype in the response to chronic Pseudomonas aeruginosa lung infection in mice. Am. J. Physiol. Lung Cell. Mol. Physiol. *287*, L944–L952.

Wang, G. (2016). Chloride flux in phagocytes. Immunol. Rev. *273*, 219–231.

Wang, X., Zhang, X., Dong, X.P., Samie, M., Li, X., Cheng, X., Goschka, A., Shen, D.,

Zhou, Y., Harlow, J., et al. (2012). TPC proteins are phosphoinositide- activated sodium-selective ion channels in endosomes and lysosomes. Cell *151*, 372–383.

Wang, W., Zhang, X., Gao, Q., Lawas, M., Yu, L., Cheng, X., Gu, M., Sahoo, N., Li, X., Li, P., et al. (2017). A voltage-dependent K(+) channel in the lysosome is required for refilling lysosomal Ca(2+) stores. J.Cell Biol. *216*, 1715–1730.

Wine, J.J. (2010). The development of lung disease in cystic fibrosis pigs. Sci. Transl. Med. *2*, 29ps20.

Zhang, Y., Li, X., Grassme, H., Doring, G., and Gulbins, E. (2010). Alterations in ceramide concentration and pH determine the release of reactive oxygen species by Cftr-deficient macrophages on infection. J. Immunol. *184*, 5104–5111.

STAR★METHODS

KEY RESOURCES TABLE

REAGENT or RESOURCE	SOURCE	IDENTIFIER
Chemicals, Peptides, and Recombinant Proteins		
Sodium bicarbonate	Sigma-Aldrich	S-5761
Sodium chloride	Sigma-Aldrich	S-9888
Sodium Methanesulfonate	Acros Organics	44211000
D-Sucrose	Fisher Scientific	BP220-212
HEPES	Sigma-Aldrich	H-4034
Potassium chloride	Sigma-Aldrich	P-4504
Potassium Methanesulfonate	Tokyo Chemical Industry Co.	M0550
D-(+)-Glucose	Sigma-Aldrich	G-8270
Magnesium chloride hexahydrate	Sigma-Aldrich	M-2393
Calcium chloride	Sigma-Aldrich	C-3881
Calcium Methanesulfonate	Tokyo Chemical Industry Co.	M0549
Choline chloride	Sigma-Aldrich	C7527
Magnesium D-gluconate hydrate	Sigma-Aldrich	G9130
DMEM + GlutaMAX -l	Gibco	10569-010
DPBS (1X)	Gibco	14190-144
CFTRinh-172	kind gift from Dr. Robert J. Bridges, Rosalind Franklin University, Chicago USA	N/A
Bafilomycin A1	Sigma-Aldrich	B1793-10UG
DMSO	Sigma-Aldrich	R10145
pHrodo Red zymosan A BioParticles conjugate	ThermoFisher Scientific	P35364
Texas Red-X, succinimidyl ester	ThermoFisher Scientific	T26536
Rhodamine Green – X, succinimidyl ester	ThermoFisher Scientific	R6113
10,10'-Bis[3-carboxypropyl]-9,9'-acridiniumdinitrate di-NHS ester (BAC-SE)	EMP Biotech GmbH	Product code: AF-0406
FM 4-64	ThermoFisher Scientific	T13320
Zymosan A BioParticles opsonizing reagent	ThermoFisher Scientific	Z2850
Zymosan A	ThermoFisher Scientific	Z2849
polydimethylsiloxane (PDMS)	The Dow Chemical Company, USA	Sylgard-184
Photoresist	MicroChem, MA USA	SU-8 2000
rabbit anti LAMP1 monoclonal primary antibody	Abcam, MA USA	RRID: AB_208943
Experimental Models: Mice/Organisms/Strains		
C57BL/6 mice	Purchased from Jackson Laboratory and bred in the University of Chicago Animal Resources Center	C57BL/6
CFTR null mice	purchased from Case Western Reserve University's Cystic Fibrosis Animal Core and bred in the University of Chicago Animal Resources Center	STOCK Cftr<tm1Unc>/ TgN(FABPCFTR)#Jaw/Cwr
CFTR null mice	purchased from The Jackson Laboratory and bred in the University of Chicago Animal Resources Center	Stock 002364
clc-3 $^{-/-}$ and *clc-3* $^{+/+}$ littermate mice	kind gift of Dr. F. Lamb (Vanderbilt University) bred in the University of Chicago Animal Resources Center	CLC3
J774A.1 cell line	American Type Culture Collection (ATCC)	TIB-67

(Continued on next page)

Continued

REAGENT or RESOURCE	SOURCE	IDENTIFIER
Software and Algorithms		
OriginPro	OriginLab Corporation	Version 2019b and 2020b
AutoCAD software	Autodesk, USA	Version 2018
ImageJ	NIH	version 1.53h
ImageJ macro	Written by V.P. Bindokas, The University of Chicago	SHG-frodo v4
Bitplane Imaris software	Andor Technology PLC	version 9.1.2
Huygens Professional for Win64	Scientific Volume Imaging B.V.	18.04. 1p0 64b
Olympus FV ASW software	Olympus USA	Version 3.0
MAPS, an IDL-based software	Written by Stefan Vogt, Martin de Jonge, Barry Lai and Joerg Maser, X-ray Science Division, Advanced Photon Source, Argonne National Laboratory, IL USA	Version 1.7.3.12
Other		
Automated Cell Counter	ThermoFisher Scientific	Countess
Parch-clamp amplifier	Molecular Devices	Axopatch 200B
Patch-clamp pipette puller	Narishige, Japan	Narishige PC-10
35 mm Glass bottom poly-D-lysine coated dishes	MatTek Corporation	P35GC-1.5-10-C
Controlled Enviroment Incubator Shaker	New Brunswick Scientific	
Plate reader	BioTek	Synergy Mx
CO2 incubator	HERAEUS	HERA Cell 150
Osmometer	Advanced Instruments Inc.	Model 3320
pH meter	HORIBA	Model LAQUA
Perti dish incubator	Harvard Apparatus	PSMI
Olympus FV1000MPE BASIC confocal microscope with CARS imaging system	Olympus USA	BX61WI
Mai Tai Fast-Tune HP DeepSee 2-photon laser	Spectra Physics	Mai Tai XF-1 DS
Leica SP5 Tandem Scanner Spectral 2-photon confocal microscope	Leica Microsystems, Inc.	TCS SP5
Oxygen plasma cleaner	Harrick Plasma, USA	Model PDC-32G
Nitrogen bomb	Parr Instrument Company, Moline, IL USA	1019 HC T304 062003 M 6332
Microfluidic flow control system	ElveFlow, France	ELVEFLOW OB1
Maskless aligner MLA150	Heidelberg Instruments Mikrotechnik GmbH, Germany	MLA150
Silicon nitride membrane windows	Silson Ltd, Southam, UK	Si_3N_4
Hard X-ray fluorescence nanoprobe	Advanced Photon Source, Argonne National Laboratory, Lemont, IL USA	Bionanoprobe at beamline 9-ID-B

RESOURCE AVAILABILITY

Lead contact

Further information and requests for resources should be directed to and will be fulfilled by lead contact Deborah J. Nelson (nelson@uchicago.edu).

Materials availability

This study did not generate new unique reagents.

Data and code availability

This study did not generate any deposited data set.

This study used only commercially available analysis code stated in the figure legends. The study did not generate or utilize any unique analysis code.

Any additional information required to reanalyze the data reported in this paper is available from the lead contact upon request.

EXPERIMENTAL MODEL AND SUBJECT DETAILS

Cell lines

The J774.1 cell line was obtained from American Type Culture Collection (ATCC).

Origin and source of the animal

CFTR null mice (STOCK Cftr<tm1Unc>/TgN(FABPCFTR)#Jaw/Cwr (van Heeckeren et al., 2004) breeding pairs were originally purchased from Case Western Reserve University's Cystic Fibrosis Animal Core. These mice are referred to in the text as $cftr^{-/-}$ and $cftr^{+/+}$. Recent new breeding pairs identical to the Case Western animals were obtained from The Jackson Laboratory, Stock 002364 as the earlier colony was observed to have lost the original $cftr^{-/-}$ phenotype as observed in Figure 2D and commented on in the text. These mice express the human CFTR protein in the gut under the influence of the rat fatty acid binding protein (FABP) promoter confined to the small gut and are referred to as "gut-corrected". The Jackson Laboratory animals have been bred as heterozygotes and initially had the same CFTR phenotype as the original Case Western Reserve animals that were bred as homozygotes. In studies examining the impact of CLC-3 expression, we used $clc\text{-}3^{-/-}$ and littermate wild type (WT) mice ($clc\text{-}3^{+/+}$) as controls. The animals were a kind gift of Dr. F. Lamb (Vanderbilt University) and have been previously described by Dickerson and colleagues (Dickerson et al., 2002).

Ethical approval

The studies, detailed herein, conform to the principles set forth by the Animal Welfare Act, and the National Institutes of Health guidelines for the care and use of a pathogen-free, biohazard level 2 facility, maintained by The University of Chicago Animal Resources Center (Chicago, IL). Care was taken to minimize the number of animals used in the study and their suffering. We understand the ethical principles under which the journal operates and our work complies with its animal ethics checklist.

Animal handling

All animals were housed in a specific pathogen-free biohazard level 2 facility maintained by The University of Chicago Animal Resources Center (Chicago, IL). Animal genotyping was performed by Transnetyx, Inc., (Cordova, TN). All animals had *ad libitum* access to chow and water. Animals were fed a standard chow diet on a standard light/dark cycle. Sex of the animals used was not considered in the present study.

Anesthetic protocols and euthanasia

Animals were deeply anesthetized by inhalation of isoflurane (4-5% isoflurane/500ml-1L/ min oxygen) with the depth of anesthesia determined by toe pinch followed by cervical dislocation.

METHOD DETAILS

Bronchoalveolar lavage from mice

Bronchoalveolar lavage (BAL) fluids were collected from euthanized mice of both sexes by flushing lungs 6 times with 0.5 ml DPBS using a blunt 16-gauge syringe needle inserted into the trachea without tearing tracheal walls. The total number of AMs (20-40 μm size) recovered from BAL depended on the genotype and ranged from approximately $0.4\text{-}1.2 \times 10^4$ per mouse. Cells were cultured on Poly-D-lysine coated, glass bottom culture dishes (MatTek Corporation, Ashland, MA) for periods of up to two weeks, in DMEM (Gibco, Life Technology Corporation, USA), 10% FBS, 1% (vol/vol) penicillin-streptomycin, and imaged in HEPES-buffered artificial cerebrospinal fluid (ACSF) solution containing (in mM): 125 NaCl, 2.5 KCl, 10 HEPES, 1.5 $MgCl_2$, 2.5 $CaCl_2$, 10.0 glucose, and 10 sucrose to adjust osmolarity to 290 mOsm, pH 7. In experiments requiring preincubation in 0 mM Cl^-, the Cl^- in ACSF was replaced by the impermeant anion methanesulfonate. All Cl^--clamping experimental solutions in Figures 2 and 3, eliminated Na^+ by replacing it with K^+. Cl^- substitution in these solutions replaced the 140 mM K-methansulfonate with KCl to obtain desired final Cl^- concentration. For the 200 mM Cl^- solution, we added 60 mM choline chloride in addition to the 140 mM KCl. The divalent salts, 1.5 $MgCl_2$, 2.5 $CaCl_2$, as well as glucose were eliminated from the Cl^--clamping experimental solutions.

Live cell time-lapse imaging

Imaging, image processing, and data analysis were performed at the University of Chicago Integrated Light Microscopy Facility. Non-SHG images were captured with a Leica SP5 Tandem Scanner Spectral 2-photon confocal microscope (Leica Microsystems, Germany). Image processing was performed using Bitplane Imaris software v. 9.1.2 (Andor Technology PLC, North Ireland).

For the determination of phagosomal pH changes, AMs were exposed to zymosan particles conjugated to a variety of fluorophore combinations, depending upon experimental goals, and including: pHrodo Red; pHrodo Red and Rhodamine Green, as well as Texas Red (Molecular Probes, Life Technology Corporation, USA) and 10,10'-Bis[3-carboxypropyl]-9,9'-acridiniumdinitrate (BAC) (emp BIOTECH GmbH, Germany). Phagocytosed zymosan particles were imaged every 1 min for up to 30 min. CFTR channel inhibitor CFTRinh-172 was a kind gift from Dr. Robert J. Bridges, Rosalind Franklin University, Chicago USA. The fluorescent particles were traced offline, and changes in fluorescence intensities were analyzed using Bitplane Imaris software. In all experiments where phagocytosis was investigated, experiments were carried out at 37°C. Experiments using live cell confocal microscopy were carried out on a heated stage enclosed in a gas-controlled chamber.

Second-harmonics generation (SHG) imaging

Live cell imaging of AMs and J774.1 cells exposed to zymosan particles was performed using an upright Olympus FV1000MPE BASIC microscope with CARS imaging system. A Spectra Physics Mai Tai Fast-Tune HP DeepSee Laser tuned to 900 nm was used for laser excitation. For cells loading FM 4-64 (50 μM) was added to cell culture media and incubated for 15 min at +37C; before imaging the media was replaced with ACSF. Time-lapse image acquisitions were done at 37°C maintained with PSMI petri dish incubator (Harvard Apparatus, Holliston, MA, USA) and image acquisition started after adding zymosan particles conjugated with the pHrodo Red fluorophore (Molecular Probes, ThermoFisher Scientific) to the cells. Images were acquired in a volume time series at a resolution of 512 x 512 pixel resolution at 0.198 μm/pixel and total image size of 101.178 μm x 101.178 μm. The Olympus XLPLN 25X W NA 1.05 MP Objective was used for observing the cells. The series was acquired with a scan rate of 8 μs/pixel scan rate with a Line Kalman filtering average of 2 and an optical zoom of 5x. The Mai Tai laser was tuned to 3% laser power mode-locked at 900 nm. Two channels were used for emission detection. One reflected non-descanned detector (NDD) Photo Multiplier Tube (PMT) was used to collect the emission of pHrodo Red with a band pass emission filter of 575 – 630 nm. The PMT was set to analog integration mode at 655 V. The other channel for emission detection was the forward or transmitted mode of detection. This detection of the transmitted signal implemented an NDD PMT. This signal was acquired through a 1.45NA oil top lens condenser. The emission of the SHG detection of FM 4-64 in the transmitted mode was collected through a band pass filter of 420 - 460 nm. The voltage on this PMT was set to 750V. Little cell damage was seen with the IR laser set at 12% laser power on the accousto-optical modulator (AOM) or below. The images were acquired at 12 bit depth. Images were acquired following the following the addition of the zymosan particles. Obtained images were analyzed and converted to TIFF formats for later analysis using Olympus FV ASW 3.0 Software.

SHG image analysis

A customized ImageJ software (NIH) macro was written (V.P. Bindokas, University of Chicago, Chicago, IL) to create circular ROI masks by measuring FM4-64 fluorescence in manually tracked phagosomes. The ROI masks allowed the investigator to measure area-integrated intensities only from the phagosomal membranes outlined by incorporated FM4-64 dye. The ROI masks were used to measure area-intergrated intensities in two channels: FM 4-64 fluorescence and SHG. The recorded channel intensity values were used to calculate the signals intensity ratios (SHG/F) during phagosomal tracking time.

Electrophysiology

Whole cell recordings in SHG voltage calibration. The voltage dependence of the FM 4-64 generated SHG/F ratio signal was obtained with a combination of whole cell patch-clamp and SHG microscopy. Whole-cell recordings were obtained using an Axopatch 200B patch-clamp amplifier (Molecular Devices) and uncoated borosilicate glass pipettes. Pipettes were pulled on a Narishige PC-10 pipette puller with resistances of 6-8 MOhm. Currents, which were not analyzed for this study, were low-pass filtered at 2.8 kHz with an 8-pole Bessel filter and digitized at 10 kHz. Recordings were made from visually identified

AMs or J774 cells at +37°C, at V_h = −40 mV. The extracellular bath solution contained (in mM): 125 NaCl, 2.5 KCl, 10 HEPES, 1.5 $MgCl_2$, 2.5 $CaCl_2$, 6 D-glucose, 28 Sucrose to adjust osmolarity to 310 mOsm, pH 7.3 was adjusted with NaOH (Na extracellular solution). The patch pipette contained (in mM): 135 KCl, 4 NaCl, 1 $MgCl_2$, 10 HEPES, 2 Mg-ATP pH 7.2 adjusted with KOH, osmolarity adjusted to 280 mOsm with Sucrose.

Microfluidic chip design and fabrication. The microfluidic platform design was based on (Skelley et al., 2009) and was modified for macrophage studies. Cells in suspension were introduced into the microfluidic chamber via the inlets and followed the channel until they reached the cell capture area where the weir-based PDMS passive cell traps are designed to isolate single cells. The cell traps feature a narrow (10μm) slit that allows fluid flow to pass around the trapped cell without disturbing the culture as well as allowing non-internalized zymosan particles to be washed away. The trap has a length of 40 μm, which deters additional cells from being trapped as well. Each chip contains 1 cell culture chamber with dimensions of 2 mm X 1.5 mm X 70 μm. The device has a total volume of ∼12.7 μl per channel. The microfluidic chip was designed using AutoCAD 2018 software (Autodesk, USA). The master molds for the chip were fabricated by patterning photoresist spin-coated on a silicon wafer using standard lithography techniques. Briefly, the master wafer was created using SU-8 2000 (MicroChem, MA USA), a negative photoresist that was spin-coated on a 3″ silicon wafer to get a 70 μm feature height. The photoresist exposure was performed with a maskless aligner MLA150 (Heidelberg Instruments Mikrotechnik GmbH, Germany) using 375 nm laser and a dose of 215 mJ/cm2. The design was then developed and polydimethylsiloxane (PDMS) (Sylgard 184 ™, The Dow Chemical Company, USA) was poured on top of the molds. PDMS was prepared by mixing the two components in a 10:1 ratio and were poured onto the dust-free wafer, de-bubbled in a desiccator, and incubated overnight at +80°C. After curing, the chips were peeled off the master and inlet and outlet ports were punched out using a 0.35 mm biopsy punch (WellTech Labs., Taiwan). The PDMS chip was then irreversibly bonded to a glass microscope 25 mm cover slip using an oxygen plasma cleaner (Harrick Plasma, USA) followed by incubation at +85°C for 2 hrs.

Microfluidic cell loading. Before introducing cells into the microfluidic chamber, the device was washed with ethanol (500 μl), followed by PBS. Finally, each chip was coated overnight with Poly-L-lysine, which helped the cells to adhere to the glass surface. The devices were then washed with sterile PBS followed by fresh medium prior to the introduction of cells. Using a loading density of 1x10^5 cells/ml, cells were introduced at a volumetric flow rate of 20 μl/min for a period of 90 seconds, allowing the isolation of single cells with over 80% efficiency. Cell traps allowed single cells to be retained within the device while free-floating cells were flushed out due to the constant perfusion. After loading cells, the perfusion was turned off and cells were allowed to rest for a minimum of 1 hr before media change thereby allowing cells to firmly adhere to the surface. After the initial cell seeding, the microfluidic device could be maintained at 37°C, 95% O_2/5% CO_2 in static cell media as long as the media was changed at 6 hr intervals throughout the day. Using this protocol, cells remained adherent to the glass and could be washed, cultured, and chemically stimulated for up to 9 days.

Nitrogen cavitation on microfluidic chip. A modified version of the standard nitrogen cavitation procedure was performed since cells were already seeded in the microfluidic device. In general, cells were kept in the microfluidic chamber for a minimum of 3 days before cavitation was performed. Cells were incubated with 0 mM Cl⁻ HEPES buffered saline for 10 min prior to addition of pHrodo-conjugated zymosan. The microfluidic devices were then incubated at 37°C for 30 min in order to allow the cells to phagocytose the zymosan particles. Non-internalized zymosan particles were then removed via flushing of the devices with 0 mM Cl⁻ solution before switching the solution to iced disruption buffer and placing all microfluidic devices on ice. The nitrogen cavitation was performed in a pressurized nitrogen bomb (Parr Instrument Company, IL USA) outfitted with a solid base within the sample compartment of the bomb. Care was taken to place the microfluidic devices on top of this solid base; otherwise, the increase in pressure would break the coverslip of the device. Once the device was placed inside the sample compartment of the bomb, PBS was poured inside the compartment until it barely covered the microfluidic device. This step was crucial in order to prevent air bubbles from forming within the gas permeable PDMS. Finally, the nitrogen bomb was sealed and the nitrogen partial pressure was increased to 400 psi and the device with cells incubated for 10 min. The quick release of pressure that follows this procedure allowed the disruption of the cells within the microfluidic device without disrupting the microchannel. After the cavitation was performed, the inlets and outlets of the device were connected to a pressure-driven microfluidic flow control system (ElveFlow, France) coupled with a flow rate control system. Flow rate was kept between 5-10 μl/min for the duration of

the experiment. Once the microfluidic device was placed on the microscope for imaging, cells were equilibrated for 5-10 min before images were taken and they were exposed to any stimuli.

Specimen preparation for hard X-ray cryo-microscopy. AMs from $cftr^{+/+}$ and $cftr^{-/-}$ mice were isolated from murine BAL. The isolated AMs were cultured on silicon nitride membrane windows (Si_3N_4, Silson Ltd, Southam, UK) with an etched grid to aid in localization following rapid freezing, and incubated in DMEM with Gluta-MAX supplemented with 10% fetal bovine serum and 1% penicillin and streptomycin to allow cells to adjust to the medium and adhere. Non-adherent or temporarily-adherent cells were removed by washing. After 2 days in culture, pHrodo-Red conjugated zymosan particles were added to the cells for 5 and 30 min. The Si_3N_4 windows with cells were briefly washed with DPBS and diH_2O, excess liquid was removed with filter paper, then plunge frozen in liquid ethane and subsequently transferred to liquid nitrogen where they were kept for the duration of all experimental procedures.

Hard X-ray microprobe and allocation of the phagosome. Hard X-ray microprobe measurements were carried out at the Argonne National Laboratory, Lemont, IL. Experiments utilized the Bionanoprobe, a hard x-ray fluorescence nanoprobe with a cryogenic sample environment that is located at beamline 9-ID-B of the Advanced Photon Source. For X-ray fluorescent signals collection incident photons of 8.2 keV were selected with a Si(111) double-crystal monocrystal, then focused down to <100 nm with zone plate optics onto a frozen sample. A full x-ray fluorescence spectrum was recorded using an energy dispersive detector (Figure 5A, XRF detector) as a 2D elemental maps (Chen et al., 2015). The data were analyzed using MAPS, an IDL-based software developed in house (Twining et al., 2003).

Reagents. All hydrophobic compounds were dissolved in dimethylsulfoxide (DMSO) as 10 mM stock solutions, while final dilutions into aqueous solutions were made just prior to use. Aliquoted stock solutions were stored at −20°C, thawing only once before use. Care was taken to use only anhydrous DMSO to avoid compound precipitation upon thawing. To further ensure solubilization of the hydrophobic test compounds, we sonicated the stock solutions for 10-15 min, prior to dilution. Chemicals were obtained from Sigma-Aldrich, USA.

QUANTIFICATION AND STATISTICAL ANALYSIS

Data in the text are presented as the mean +/− standard error of the mean with the number of particles, cells, or animals in parentheses or stated in the figure legends. Analysis of the statistically significant difference between groups, One-Way ANOVA analyses (Tukey Test) were performed using OriginPro 2020b software (OriginLab Corporation, USA). Statistical differences were assumed to be significant when $p < 0.05$. No randomization or blinding procedures were used in the experiments. Mathematical fits to the data are described in the figure legends.